Journal of Structural Geology 203 (2026) 105584

Contents lists available at ScienceDirect

Journal of Structural Geology

journal homepage: www.elsevier.com/locate/jsg

Hydrolytic weakening controls Jurassic to early Cretaceous mylonitisation in the basement of the Pyrenees

Eloi González-Esvertit [a,b,*], Josep Maria Casas [c], Àngels Canals [a], Paul D. Bons [d,e], Kevin Konrad [f], Maria-Gema Llorens [b], Gabriel Serrano-López [g], Claudia Prieto-Torrell [a,b], Joyce Neilson [h], Diego Domínguez-Carretero [a], Aratz Beranoaguirre [i,j], Axel Gerdes [i,j], Enrique Gomez-Rivas [a]

[a] Departament de Mineralogia, Petrologia i Geologia Aplicada, Facultat de Ciències de la Terra, Universitat de Barcelona, 08028, Barcelona, Spain
[b] Geosciences Barcelona, GEO3BCN-CSIC, 08028, Barcelona, Spain
[c] Departament de Dinàmica de la Terra i l'Oceà, Facultat de Ciències de la Terra, Universitat de Barcelona, 08028, Barcelona, Spain
[d] Department of Geosciences, Tübingen University, 82076, Tübingen, Germany
[e] School of Earth Science and Resources, China University of Geosciences (Beijing), 110083, Beijing, China
[f] College of Earth, Ocean and Atmospheric Sciences, Oregon State University, OR, 97331, Corvallis, USA
[g] Institut des Sciences de la Terre d'Orléans (ISTO), CNRS-BRGM, Universite d'Orleans, UMR 7327, 45071, Orleans, France
[h] School of Geosciences, King's College, University of Aberdeen, AB24, 3UE, Aberdeen, United Kingdom
[i] Institut für Geowissenschaften, Goethe-Universität Frankfurt, 60438, Frankfurt am Main, Germany
[j] Frankfurt Isotope and Element Research Center (FIERCE), Goethe-Universität Frankfurt, 60438, Frankfurt am Main, Germany

ARTICLE INFO

Keywords:
$^{40}Ar/^{39}Ar$ geochronology
U-Pb geochronology
Quartz CPO
Quartz mylonite
Pyrenees

ABSTRACT

The age of the mylonite belts in the basement rocks of the Pyrenees is a subject of debate in the structural geology and petrology communities because of its potential implication on the regional tectonothermal history and on the tectonic evolution of SW Europe. Here we address when and how mylonitisation took place in two key areas of the Eastern Pyrenees, where shear zones are associated with Giant Quartz Veins (GQVs). We conducted zircon U-Pb and muscovite $^{40}Ar/^{39}Ar$ dating coupled with structural, textural, and crystallographic preferred orientation (CPO) analyses of mylonites from the Cap de Creus and Canigó Massifs. U-Pb zircon dating of a dacite porphyry dyke crosscut by GQVs and mylonitic bands yields a maximum shear zone and GQV formation age of ca. 292 ± 3 Ma. $^{40}Ar/^{39}Ar$ analyses of muscovite within mylonitised GQVs yield initial crystallisation ages between ca. 164 and 188 Ma, as well as younger recrystallisation ages of ca. 110–118 Ma. A qualitative assessment of the GQV history is inferred from step-heating spectra of muscovite and quartz CPOs. The results indicate that GQV formation and mylonitisation were coupled, coeval, and long-lasting processes that took place from early Jurassic to early Cretaceous times. A comparative evaluation of quartz CPOs reveals inconsistencies regarding the strain distribution, quartz slip systems activity, and deformation temperatures depending on the deformed rock type. Quartz mylonites have stronger CPOs dominated by basal <a>, prism <a>, or prism <c> slip systems, whilst phyllonites and granite mylonites show weaker fabrics mostly dominated by mixed <a> slip. This apparently suggests higher deformation temperatures in quartz mylonites than those inferred from more reliable proxies, such as mineral assemblages, brittle behaviour of K-feldspar, and fluid inclusion data. We suggest that the water-weakening effect caused by coeval formation and deformation of GQVs enabled easier dislocation glide and creep, allowing strain localisation and transitions between slip systems at lower temperatures than commonly inferred due to enhanced ductility. U-Pb zircon dating further suggests the existence of an early Carboniferous (ca. 332 ± 4 Ma; Visean) magmatic episode in the Pyrenees, in agreement with a cyclic, rather than a progressive, geodynamic history of the region during Variscan times. The present work challenges classical interpretations stating that Pyrenean mylonite belts developed during the retrograde stages of the Variscan Orogeny, highlighting that the structural evolution of this region during Mesozoic times deserves further investigation. Results have implications for interpreting deformation localisation mechanisms and conditions in crustal rocks, for the formation mechanisms of GQVs in worldwide orogenic belts, and for the tectonothermal history of the Pyrenees since late-Variscan times.

* Corresponding author. Departament de Mineralogia, Petrologia i Geologia Aplicada, Facultat de Ciències de la Terra, Universitat de Barcelona, 08028, Barcelona, Spain.
E-mail address: e.gonzalez-esvertit@ub.edu (E. González-Esvertit).

https://doi.org/10.1016/j.jsg.2025.105584
Received 14 July 2025; Received in revised form 7 November 2025; Accepted 10 November 2025
Available online 12 November 2025

1. Introduction

Deformation localisation — the concentration of strain within specific sectors in a deforming material — results in the formation of shear zones at all scales within the Earth's crust (Ramsay and Graham, 1970; Sibson, 1977; Lister and Williams, 1979, 1983; Simpson and De Paor, 1993; Carreras, 2001; de Riese et al., 2019) and mantle (Vissers et al., 1995; Skemer et al., 2010; Vauchez et al., 2012). From the sub-millimetre to the kilometre scale, these zones represent rheological and mechanical anomalies due to changes in deformation mechanisms, grain size, and crystallographic preferred orientation (CPO), among others, when compared to undeformed materials (Hirth and Tullis, 1992; Keulen et al., 2007; Toy et al., 2008; Finch et al., 2016; Cawood and Platt, 2021). Accordingly, they potentially control subsequent deformation processes, fluid flow, partial melting, magma emplacement and, overall, the strength of the lithosphere (McCaig et al., 1990; Neves et al., 1996; Bürgmann and Dresen, 2008; Salomon et al., 2015; Cao and Neubauer, 2016; Lee et al., 2020).

Factors controlling deformation localisation and shear zone initiation in a given rock type are those that induce intrinsic (i.e., crystal) or composite anisotropy into that rock at multiple scales (e.g., mineralogical, compositional and grain size variations, pre-existing brittle and ductile structural heterogeneities, and presence of fluid or melt; Pennacchioni and Cesare, 1997; Mandal et al., 2004; Griera et al., 2011; Pennacchioni and Zucchi, 2013; Bons et al., 2016; Fossen and Cavalcante, 2017; Llorens et al., 2019; Ran et al., 2019). Deformation is preferentially localised along mechanically weak areas that show favourable orientations with respect to the stress field that the rock is subjected to. Areas with abundant weak mineral phases, such as micas, where shearing along the crystal basal plane occurs more easily than in any other direction, or those containing pre-existing cracks or fracture sets, are examples of such mechanical weakness. In the Pyrenees (SW Europe) however, the ubiquitous occurrence of mylonite belts that sometimes show deformation localisation along Giant Quartz Veins (GQVs; i.e., veins with widths up to tens of meters and lengths of kilometres) appear to contradict this phenomenon (González-Esvertit et al., 2022a, 2022b, 2024). Therefore, the first problem we aim to address here is why deformation localisation occurs within the GQV quartz, and why strain apparently increases towards the GQV cores, assuming quartz represents a harder phase than the surrounding, often mica-rich, host rock.

Moreover, although the timing of most of the tectonometamorphic and magmatic events recorded in the basement rocks of the Pyrenees seems to be well constrained (e.g., Autran et al., 1970; Santanach, 1972a; Deloule et al., 2002; Casas et al., 2010; Castiñeiras et al., 2011; Aguilar et al., 2014; Navidad et al., 2018; Lemirre et al., 2019; Liesa et al., 2021; Caldera et al., 2023), the age of these mylonite belts and associated GQVs remains controversial (Carreras et al., 1980; Soula et al., 1986; Laumonier et al., 2015; Vissers et al., 2017, 2020; Druguet et al., 2018; Pitra and Martínez, 2024; González-Esvertit et al., 2024; Monié et al., 2025). Several models have interpreted these shear zones as late-Variscan structures formed during progressive ductile deformation (e.g., Fusseis et al., 2006; Druguet and Carreras, 2019), although recent geochronological data suggest Jurassic (Vissers et al., 2017) or Eocene (Vissers et al., 2020; Monié et al., 2025) shear zone activity. Recently, the formation of shear zone-related GQVs has been interpreted as a low temperature (<200 °C), long-lasting process occurring through continuous or successive pulses of heat, fluid, and mass supply, which resulted in the development of extensive metasomatic haloes involving silicification and mineral replacement reactions (González-Esvertit et al., 2024, 2025a, 2025b). Accordingly, the second problem here addressed is the timing and formation conditions of the mylonite belts and of the associated GQVs.

We address these gaps by investigating, across scales, two localities famous among structural geologists and petrologists due to the exposure of ductile deformation structures and metasomatic rocks: the Cap de Creus Massif, where shear zones have classically been described as areas of inhomogeneous deformation (e.g., White et al., 1980; Carreras, 2001; Llorens et al., 2013), and the Canigó Massif, where particular rock types and mineralogical changes (i.e., silicification, feldspathisation, and muscovitisation) have attracted attention for more than a century (Michel-Lévy, 1889; Lacroix, 1896, 1898, 1920; Adams, 1901; Guitard, 1953, 1955; Casas, 1984, 1986; González-Esvertit et al., 2025c) (Fig. 1). Because both areas record similar histories of sedimentation, magmatism, metamorphism, and brittle-ductile deformation, they offer an exceptional opportunity for direct comparison and correlation. The results provide new insights into deformation localisation processes and their controlling factors in crustal domains, as well as into the formation mechanisms of GQVs and the tectonothermal evolution of the Pyrenees since late-Variscan times.

2. Geological setting

The Pyrenees (Fig. 1) is a doubly verging, E-W-trending Alpine fold-and-thrust belt that formed due to the collision between the Iberian and Eurasian plates from the late Cretaceous to Miocene (e.g., Roest and Srivastava, 1991; Muñoz, 1992; Macchiavelli et al., 2017; Vergés et al., 2019). Alpine deformation resulted in the exhumation of late Neoproterozoic-to-Carboniferous basement rocks along the backbone of the cordillera (Axial Zone), which is composed of metasediments, Variscan (Carboniferous) orthogneisses derived from late Neoproterozoic and Ordovician intrusives, and late-Variscan granitoids (Fig. 1). These rocks further record Sardic (Ordovician), Variscan, and Alpine polyphase deformation, as well as Variscan regional metamorphism (Santanach, 1972b; Carreras et al., 1980; Muñoz, 1992; Casas, 2010; Padel et al., 2018; Martín-Closas et al., 2018; Navidad et al., 2018; Puddu et al., 2019; Liesa et al., 2021; Margalef et al., 2023).

Several mylonite belts present throughout the basement rocks of the Eastern Pyrenees have gained significant attention due to their implications in tectonic plate reconstructions and the deformation history of the region (Autran and Guitard, 1968; Carreras et al., 1980, 2004a; Casas, 1984, 1986; Simpson, 1985; McCaig and Miller, 1986; Carreras and Cirés, 1986; Soula et al., 1986; Liesa and Carreras, 1989; McCaig et al., 1990, 2000a, 2000b; Monie et al., 1994; Maurel, 2003; Auréjac et al., 2004; Vilà et al., 2007; Denèle et al., 2008; Mezger et al., 2012; Olivier et al., 2016; Le Bayon and Cochelin, 2020; Barrón, 2023). They are formed by anastomosing shear zones affecting either metasedimentary sequences, orthogneisses, or granitoids, with gently to steeply dipping mylonitic foliations and associated stretching lineations. These mylonite belts have classically been attributed to late-Variscan tectonics (e.g., Druguet, 1997; Carreras, 2001; Carreras et al., 2004a; Mezger et al., 2012), although no consensus has been reached yet on their tectonic significance, since they have been interpreted as formed under extensional, compressional, or transpressional regimes (e.g., Carreras and Capella, 1994; Druguet, 1997; Carreras, 2001; Denèle et al., 2008; Le Bayon and Cochelin, 2020). Noteworthy, some of them are spatially related to steeply- or subvertical-dipping GQVs (González-Esvertit et al., 2022a, 2022b, 2023) that have been interpreted as products of large-scale mineral replacement during coupled Si-metasomatism and deformation in the Canigó (González-Esvertit et al., 2025a, Fig. 2) and Cap de Creus Massifs (González-Esvertit et al., 2022b, Fig. 3).

The Canigó Massif (Fig. 1 and Fig. 2) is an E-W-trending antiformal macrostructure in the Eastern Pyrenees that exposes a 3000 m-thick package of Variscan orthogneisses (Canigó gneisses; Guitard, 1965,

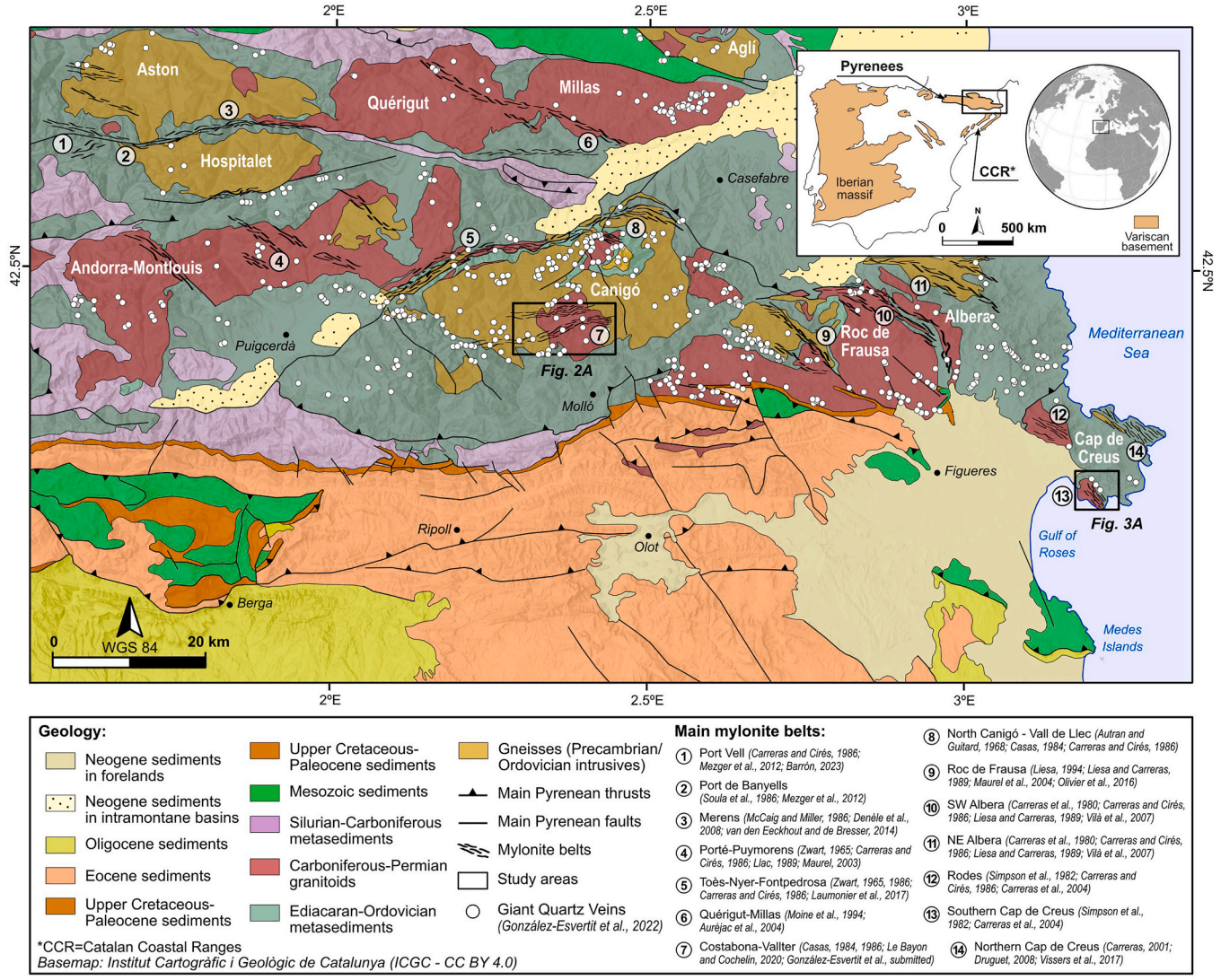

Fig. 1. Geological map of the Eastern Pyrenees (SW Europe) (EPSG:4326) with the location of the main mylonite belts reported in the literature. The spatial distribution of Giant Quartz Veins as reported in González-Esvertit et al. (2022a) is also included. (For interpretation of the references to colour in this figure legend, the reader is referred to the Web version of this article.)

1970; Autran and Guitard, 1968; Casas, 1984; Navidad et al., 2018) derived from Ordovician granitic intrusives (464–457 Ma; SHRIMP U-Pb in zircon; Navidad et al., 2018 and the references therein), which are intercalated in a ca. 4000 m-thick pre-Upper Ordovician metasedimentary sequence. This metasediments are mainly composed of low-to-high grade mica schists and metapelites with intercalations of marble, quartzite, metabasite, and felsic metatuff layers (Guitard, 1953; Laumonier, 1988; Casas et al., 2010; Padel et al., 2018). In the core of the massif (Fig. 2), a late-Variscan peraluminous biotite-bearing monzogranite (Costabona monzogranite; 302 ± 4 Ma; LA-ICP-MS U-Pb in zircon; Laumonier et al., 2015) postdates a polyphase Variscan deformation event (late Tournaisian to early Kasimovian) and the Variscan regional metamorphism that affected the surrounding metasediments and orthogneisses (Autran et al., 1970; Guitard, 1970; Casas, 1984; Zwart, 1986). In the central area of the Canigó Massif, the Costabona-Ulldeter mylonite belt exhibits a E-W- to ENE-WSW-trending and NNW-dipping mylonitic foliation that crosscuts the Canigó granitic orthogneisses (Guitard, 1965, 1970; Autran and Guitard, 1968; Casas, 1982, 1984, 1986), the Costabona monzogranite (Guitard et al., 1998; Laumonier et al., 2015), and the GQVs (González-Esvertit et al., 2025a) (Fig. 2 and Fig. 4). This mylonite belt is thus younger than the Canigó granitic orthogneisses (ca. 464–457 Ma) and the Costabona monzogranite (ca. 302 ± 4 Ma).

The Cap de Creus Massif (Fig. 1 and Fig. 3) is located at the eastern end of the Pyrenean Axial Zone. It exposes a late Neoproterozoic-Cambrian (Castiñeiras et al., 2008a) metasedimentary succession composed of siliciclastic rocks with metabasite and minor carbonate levels that record Variscan LP-HT metamorphism. Two main rock units can be differentiated in the southern sector of the Cap de Creus: the late Neoproterozoic Lower Series (i.e. Cadaqués and Montjoi Series) and the early Cambrian Upper Series (i.e. Norfeu Series) (Druguet et al., 2014; Casas et al., 2015; Druguet and Carreras, 2019). A ca. 30 m-thick unit of felsic volcanic rocks is interbedded within the Lower Series metasediments (Mas de la Torre acid metatuffs; 558 ± 3 Ma; LA-ICP-MS U-Pb in zircon; Casas et al., 2015, Fig. 3). The metamorphic grade of these rocks increases from lower-greenschist to amphibolite facies (± cordierite and sillimanite, up to migmatite-grade) towards the NE of the massif (Druguet, 1997; Carreras, 2001), where the El Port orthogneiss (553 ± 4 Ma; SHRIMP U-Pb in zircon; Castiñeiras et al., 2008a) also crops out. Successive deformation episodes are registered by fold superposition, the development of three main cleavage generations, and an exceptionally well exposed set of regional-scale ductile shear zones (Fig. 4).

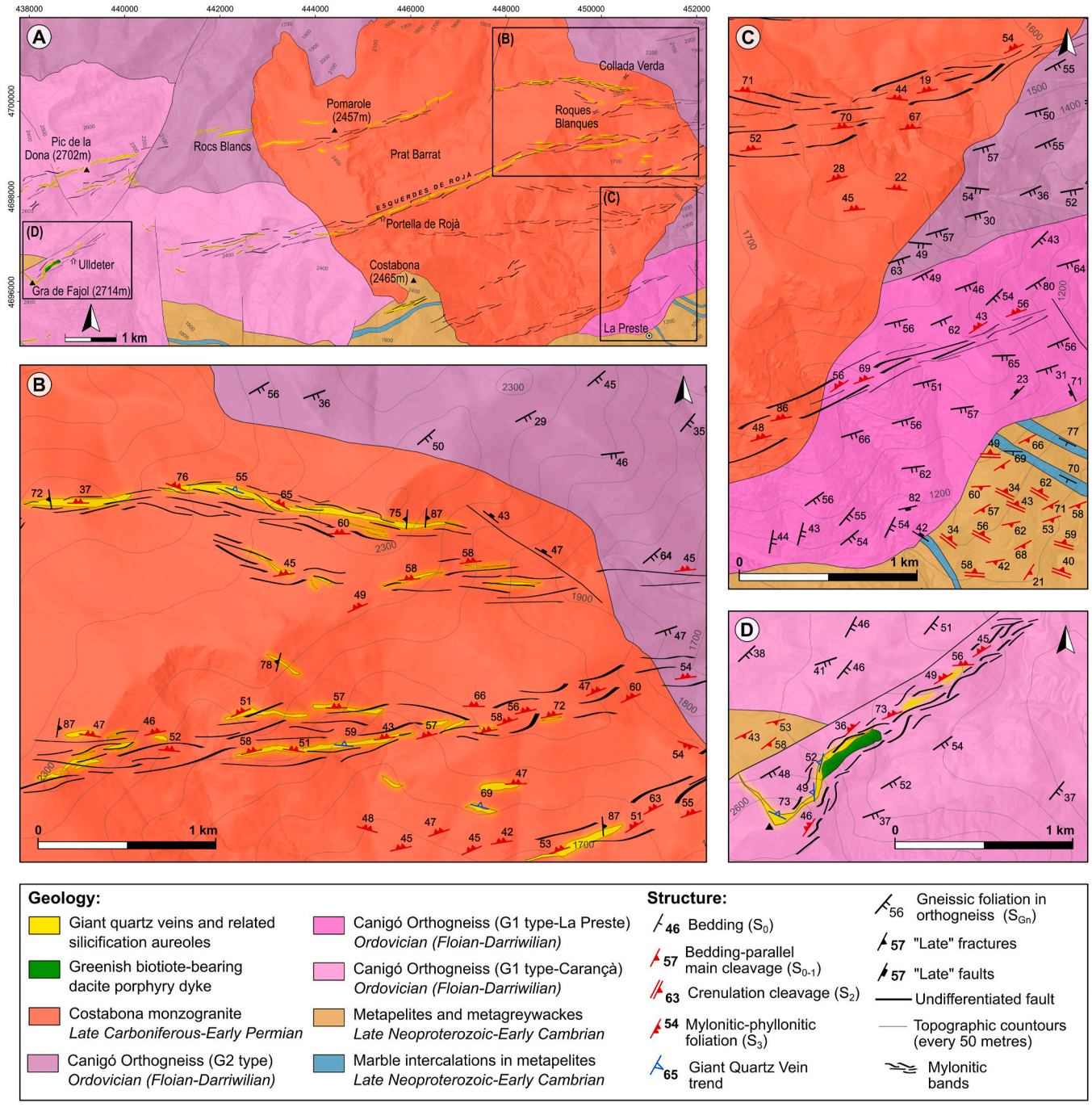

Fig. 2. Geological map of the study area in the Canigó Massif (EPSG:32631) (A), zooming on the structural details of the Collada de Roques Blanques (B), La Preste (C), and Ulldeter (D) sectors. Mapping and structural analysis were carried out in the whole area shown in (A), but only sectors (B–D) are shown here in detail for clarity. See location in Fig. 1. (For interpretation of the references to colour in this figure legend, the reader is referred to the Web version of this article.)

These shear zones are generally oriented NW-SE and crosscut the rest of the amphibolite facies Variscan macrostructure along the northern and southern parts of the massif (Carreras et al., 1980; Carreras and Casas, 1987; Druguet, 1997; Llorens et al., 2013; Vissers et al., 2017, 2020; Druguet and Carreras, 2019). A swarm of pegmatitic granitoids is found in the northern part of the massif (e.g., Bons et al., 2004). A large, sheet-shaped granodiorite body (the Roses granodiorite) crops out in the southern sector. Both pegmatites and the granodiorite are transected by the shear zones. The timing and tectonic significance of mylonitisation in the northern shear belt has been largely addressed and debated, without reaching any consensus hitherto (Druguet, 1997; Carreras, 2001; Vissers et al., 2017, 2020; Druguet et al., 2018). The structural history of these shear zones has been traditionally interpreted as part of a progressive late-Variscan deformation sequence. According to Druguet and Carreras (2019), the dominant foliation (S0/S1) is overprinted by a second cleavage (S2), which evolves into a third phase (D3a) characterised by folding and local development of S3 surfaces, culminating in mylonitic shear zones (D3b). Pegmatites emplaced during this progressive deformation further constrain the timing of shearing to a late-Variscan stage. A slightly different model proposed by Bons et al. (2016) suggests pegmatite intrusion after D2 and prior to D3, with D3a giving rise to broad shear zones and D3b the final localised, high strain

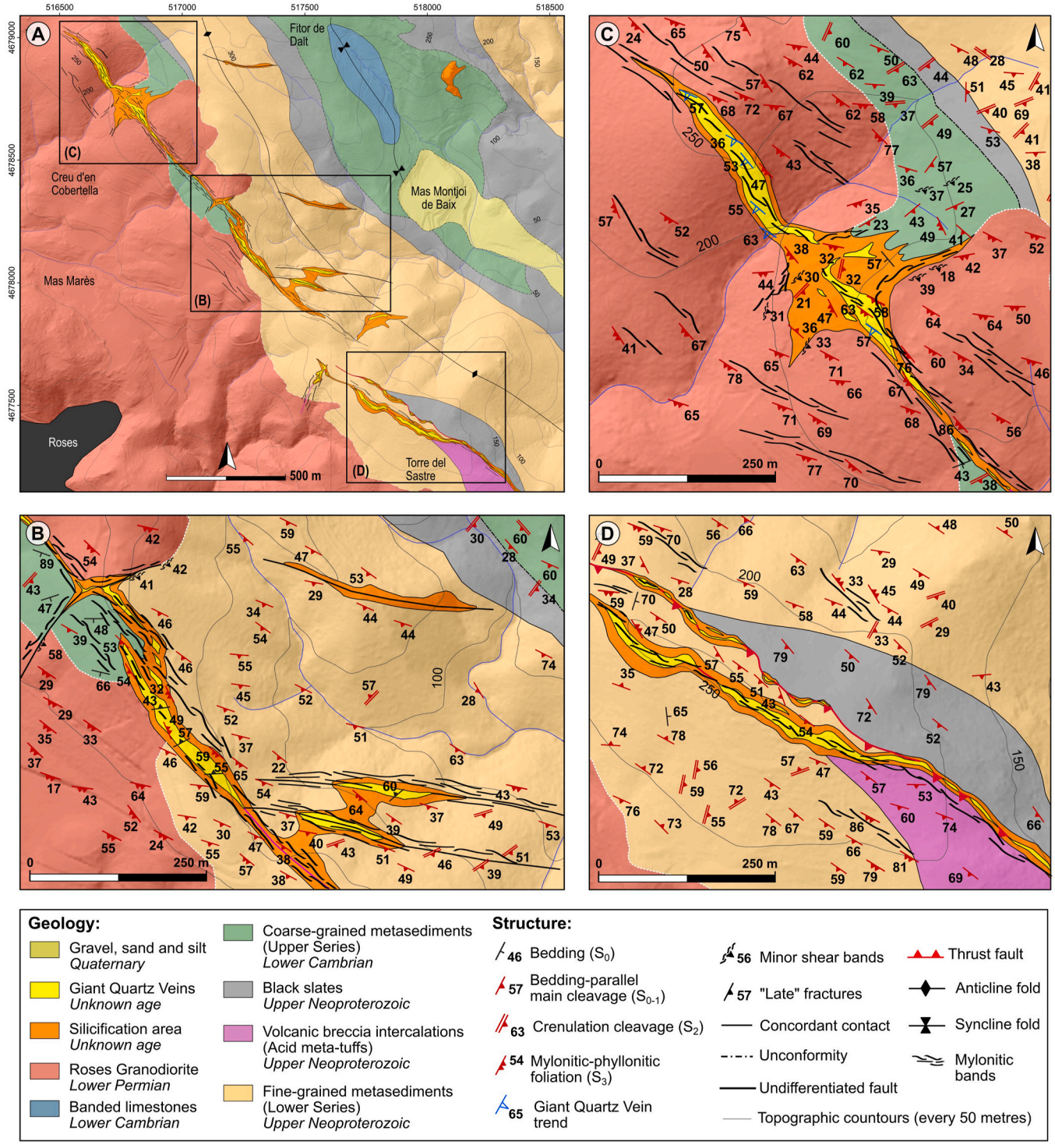

Fig. 3. Geological map of the study area in the Cap de Creus Massif (EPSG:32631) (A), zooming on the structural details of the Mas Marès (B), Creu d'en Cobertella (C), and Torre del Sastre (D) sectors. Mapping and structural analysis were carried out in the whole area shown in (A), but only sectors (B–D) are shown here in detail for clarity. See location in Fig. 1. (For interpretation of the references to colour in this figure legend, the reader is referred to the Web version of this article.)

mylonites, implying a progressive strain localisation. Additionally, Fusseis et al. (2006) suggested that these shear zones initiated as brittle faults that later evolved into ductile structures through widening. All three interpretations attribute the formation of the shear zones to late-Variscan tectonics. However, the presence of Eocene pseudotachylites within the shear zones, and younger $^{40}Ar/^{39}Ar$ ages recently obtained (e.g., Vissers et al., 2017; Monié et al., 2025) challenge this view, suggesting a more complex history that may involve significant post-Variscan shear zone activity.

3. Methods

3.1. Field methods and sampling philosophy

Detailed geological mapping (at 1:2500 scale), structural analysis, and sampling were carried out in the Canigó and Cap de Creus Massifs.

Previously published geological maps of neighbouring sectors were continuously consulted for regional comparisons (Guitard, 1970; Carreras and Losantos, 1982; Ayora and Casas, 1983; Casas, 1984; Losantos et al., 1997; Guitard et al., 1998; Carreras et al., 2004b; Laumonier et al., 2015). Orientation measurements of GQV trends, host rock bedding and cleavage planes, faults, mylonitic foliations, fold axes, and fracture sets were collected and georeferenced. Mylonitic bands affecting GQVs and host rocks were carefully examined and sampled to ensure host rock representativity and to assess microstructural differences depending on the host rock type (e.g., mineral assemblage and anisotropy). The samples are granite mylonites and quartz mylonites in the Canigó Massif (Fig. 4A–D) and phyllonites (i.e., schist mylonites) and quartz mylonites in the Cap de Creus Massif (Fig. 4E–H). Representative thin sections parallel to lineation and perpendicular to foliation (i.e., XZ-plane of the finite strain ellipsoid) were characterised under optical microscopy. Samples and thin sections originally presented in Casas (1982, 1984, 1986) and Ayora and Casas (1983) were also described and re-examined. The most promising thin sections, based on their mineral phase content and deformation microstructures, were selected for crystal orientation analyses aiming to obtain a complete assessment of brittle and ductile deformation processes in both GQVs and host rocks affected by mylonitic bands.

3.2. Electron backscatter diffraction analysis and data postprocessing

Electron backscatter diffraction (EBSD) analyses were carried out using an Oxford Instruments EBSD detector coupled to a scanning electron microscope (SEM) at the University of Aberdeen (Scotland). Thin sections were carefully polished with colloidal silica and coated with a carbon layer. Between 1 and 3 regions per thin section with distinct mineral phases and deformation microstructures were scanned under vacuum using an accelerating voltage of 20 kV at working distances ranging from 14 to 20 mm. The scanning area of each region was between 4 and 16 mm^2. Step size was set between 2 and 8.5 μm depending on scanning area and sample grain size to obtain a minimum of four indexed points per grain, with the aim of enabling comparison with other datasets collected using universal stage techniques. Grains were reconstructed from indexed EBSD patterns considering a high-angle grain boundary (HAGB) misorientation threshold of $\geq 10^\circ$, while subgrain boundaries or low-angle grain boundaries (LAGB) were defined by a 2°–10° misorientation threshold (e.g., Shigematsu et al., 2006). Recrystallised and relict grains were distinguished based on their grain orientation spread (GOS), which provides quantification for intragranular lattice distortion and acts as a proxy for dislocation density (Cross et al., 2017). One-point-per-grain pole figures were constructed within the finite strain reference frame, where the projection plane is parallel to the stretching lineation and perpendicular to the foliation. EBSD pattern indexing, data curation, and data visualisation were carried out using the AZtecHKL, AZtecOne, and AZtecCrystal software suites (*Oxford Instruments*®).

3.3. $^{40}Ar/^{39}Ar$ geochronology

Incremental heating $^{40}Ar/^{39}Ar$ age determination experiments were undertaken at the Nevada Isotope Geochronology Laboratory (University of Nevada, Las Vegas). Four muscovite samples found within relatively undeformed domains of GQVs from the Canigó Massif were analysed. Coarse muscovite was separated from the veins and packaged between Fish Canyon Tuff Sanidine fluence monitors. The samples were irradiated for 14 h at the Oregon State University TRIGA reactor. Individual separates were dropped into a double-vacuum furnace at 400 °C and exposed to a turbo pump for 2 to 3 h to remove adhered atmospheric argon. Samples were then analysed using an NGX multicollection mass spectrometer following the methods outlined in Balbas et al. (2023). The experiments consisted of 22–31 incremental heating steps with temperatures ranging from 600 to 1400 °C. The density of heating steps was systematically increased to help potentially tease out any thermal history information.

The ages were calculated using ArArCalc software (Koppers, 2002), assuming a Fish Canyon Tuff Sanidine age of 28.201 ± 0.023 Ma (Kuiper et al., 2008) and $^{40}K\ \lambda_{total} = 5.53 \pm 0.048 \times 10^{-10}\ a^{-1}$ (Min et al., 2000). All age determinations shown are reported at the 2σ uncertainty level calculated according to Balbas et al. (2023). Data and metadata related to the analysed samples and to the sample irradiation, incremental heating, $^{40}Ar/^{39}Ar$ measurements, and age calculations are reported in the Supplementary Material 1 (SM1), fulfilling the requirements acknowledged in Schaen et al. (2020).

3.4. Zircon U-Pb geochronology

Zircon separation was carried out in a dacite porphyry sample that is crosscut by GQVs and mylonite bands at the Ulldeter area (Fig. 2D). The sample was crushed, sieved, and processed using the hydroseparation technique (HS Lab, Universitat de Barcelona; www.hslab-barcelona.com) to obtain zircon preconcentrates. This technique, following the methodology proposed by Aiglsperger et al. (2015) and subsequently used to concentrate different kinds of high-density minerals in different geological environments (e.g., Pujol-Solà et al., 2021; Domínguez-Carretero et al., 2022), has proved to be useful at liberating and producing heavy mineral concentrates (in this case, zircons), by simulating natural beach placer deposits by a combination of a laminar water flow at constant pressure with diverse wave impulses.

Zircons were handpicked from the mineral preconcentrates and mounted on monolayers for their subsequent geochronological analysis. Cathodoluminescence (CL) and SEM images were taken before the U-Pb analysis at the FIERCE laboratory at the Goethe University Frankfurt. These CL and SEM images were used to select laser ablation spot locations. The selected zircon grains were analysed using an ArF excimer laser equipped with a two-volume ablation cell (RESOlution, COMpex Pro 102) coupled to a single collector inductively coupled plasma mass spectrometer (ElementXR, ThermoScientific). Prior to the analysis, the instruments were tuned for maximum sensitivity following Beranoaguirre et al. (2022). The GJ1 zircon (Jackson et al., 2004) was used as primary reference material, while BB-16 (Santos et al., 2017) and Plesovice (Slama et al., 2008) zircon crystals were analysed for validation. The results of the reference materials and sample analyses, as well as the details of all analytical parameters are provided in the Supplementary Material 2 (SM2).

Data processing was done using an in-house Microsoft Excel spreadsheet (see more details in Gerdes and Zeh, 2006, 2009). Uncertainties reported are at the 2σ level and are calculated by the quadratic addition of the internal uncertainties (SE), counting statistics, gas-background uncertainties, common Pb corrections, and the excess of scatter derived from the primary reference material (see Horstwood et al., 2016). Expanded uncertainties, i.e., long-term reproducibility (1 % and 2σ), and the decay constant uncertainty, are also reported (SM2). Concordia ages have been calculated using Isoplot 4.15 (Ludwig, 2012).

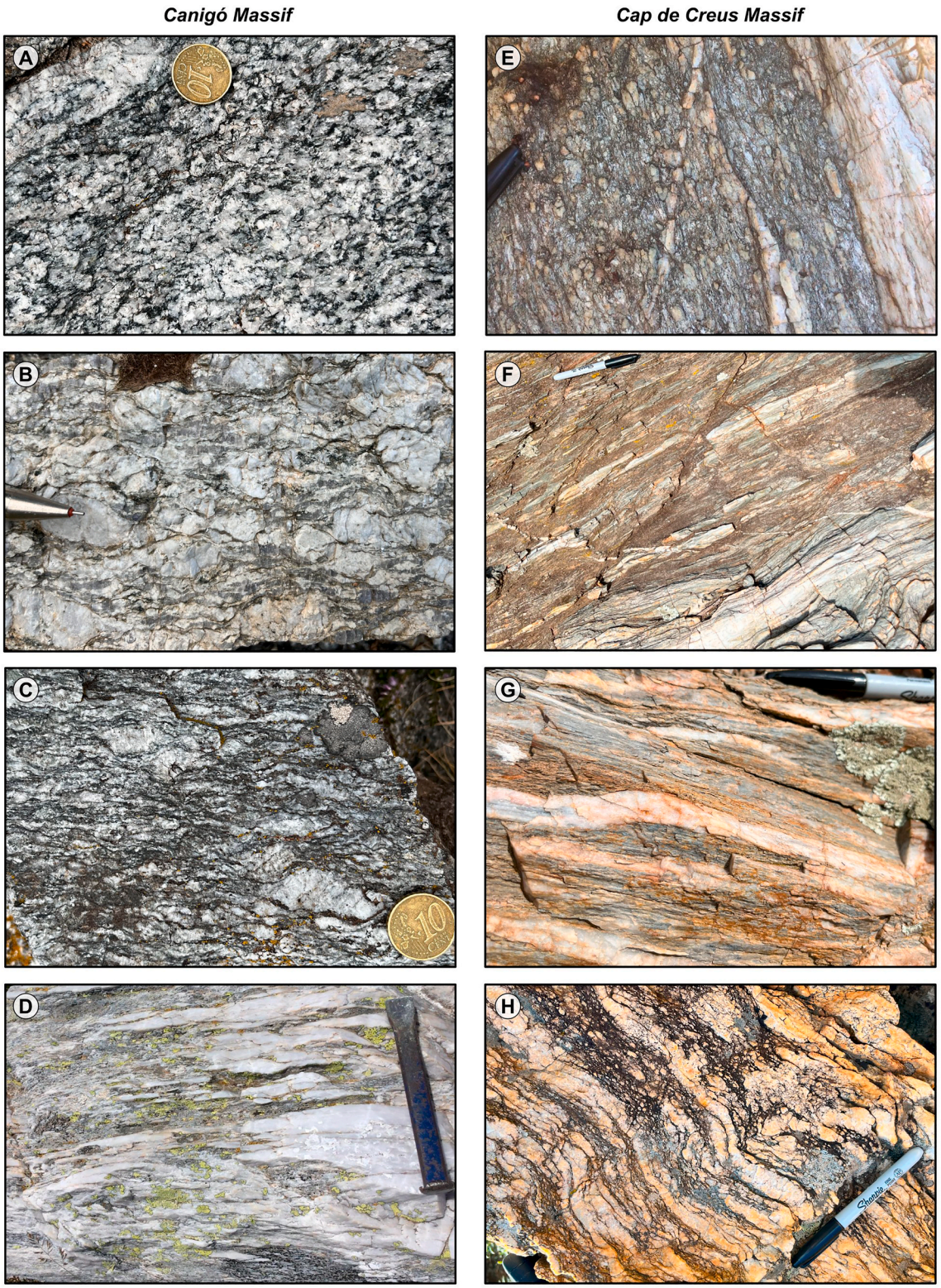

Fig. 4. Field photographs of mylonites within shear zones in the Canigó (A–D) and Cap de Creus (E–H) Massifs. (A–C) Granite mylonites from a shear zone at the Collada de Roques Blanques area (Fig. 2B), which often provide a gneissic aspect to the Costabona monzogranite. (D) Quartz mylonite from a shear zone affecting a Giant Quartz Vein, with intense and inhomogeneous development of mylonitic foliation (S_m) surfaces. (E) Granite mylonite from the Creu d'en Cobertella area (Fig. 3C), where the Roses granodiorite also acquires a gneissic texture. (F) Schist mylonite (phyllonite) in the Mas Marès area (Fig. 3B) showing quartz- and mica-rich domains where deformation is heterogeneously localised. (G, H) Quartz mylonites developing high strain domains at the Creu d'en Cobertella area (Fig. 3C); note that, in (H), cataclastic deformation overprints the mylonitic fabrics. (For interpretation of the references to colour in this figure legend, the reader is referred to the Web version of this article.)

4. Results

4.1. Large-scale structure

Low-to-mid grade mica schists and marble intercalations (Canaveilles series; Laumonier, 1988; Guitard et al., 1998; or Canaveilles Group; Padel et al., 2018) are present at the southern sector of the study area in the Canigó Massif (Fig. 2). Bedding surfaces (S_0) of mica schists are parallel to a NE-SW-trending cleavage ($S_{0\text{-}1}$) mainly defined by the orientation of biotite and muscovite crystals. An E-W-trending, N-dipping crenulation cleavage (S_2) associated to D_2 folds can be recognised at most outcrops (Fig. 2 and Fig. 5). Overlying the Canaveilles series, the Canigó granitic orthogneisses (types G1 and G2; Guitard, 1970; Casas, 1984) extensively crop out in the central and northern sectors of the study area. They show a SW-NE-trending gneissic foliation (S_{Gn}) dipping towards the SE, defined by biotite and muscovite crystals embedding φ- and σ-type porphyroclasts of K-feldspar and quartz. Metasediments and orthogneisses are crosscut by the Costabona monzogranite, and all three rock types are in turn crosscut by a set of WSW-ENE-trending mylonite bands parallel to GQVs and their alteration haloes. The mylonitic foliation (S_m) trends WSW-ENE to WNW-ESE and dips either towards the S or N, although S-dipping, W-E-trending surfaces are the most common (Fig. 2 and Fig. 5). Different strain domains are well exposed throughout the study area, from incipient S_m development by the alignment of some biotite crystals (Fig. 4A) to quartz recrystallisation and strong lattice preferred orientation. Low-to-mid strain domains produce a gneissic aspect of the Costabona monzogranite (Fig. 4B and C), whilst high strain domains are solely developed when S_m affects GQVs, developing quartz mylonites (Fig. 4D). In these cases, shear zones are usually thin (2–10 m in width) at the map scale and the S_m surfaces are parallel to the direction of GQVs (S_{GQV}), showing a more intense clustering in the stereoplots (Fig. 5). N-S oriented brittle fractures that postdate all other structures are also present and form 1–4 cm-spaced fracture sets (Fig. 2 and Fig. 5).

A similar pattern of cleavage generations and structural configuration, but with different orientations, has been identified in the Cap de Creus Massif (Fig. 5). In the area near the Roses granodiorite (Fig. 3), the $S_{0\text{-}1}$ is the dominant mesostructure in metasediments of the Lower and Upper Series. It consists of NW-SE-oriented and SW-dipping layers with thicknesses ranging between 0.2 and 3 cm (Fig. 3 and Fig. 5), which are defined by the orientation of fine-grained phyllosilicates. S_2 surfaces consist of a NE-SW-trending and moderately SE-dipping crenulation cleavage. Pre-Variscan metasediments and the late-Variscan Roses granodiorite are postdated by NW-SE-oriented and SW-dipping GQVs (Fig. 5). These latter S_{GQV} structures are, in turn, spatially related to the heterogeneous development of mylonitic S_m surfaces. S_m forms in lower strain domains when affecting host rocks (Fig. 4E), forming granite mylonites and phyllonites, and in significantly higher strain domains when present within the GQV quartz, forming quartz mylonites (Fig. 4G and H). Strain localisation along the GQVs (i.e., more intense deformation towards the GQV centre) and shear zone widening in host rock domains is often observed at the map and outcrop scales (Fig. 3 and Fig. 4F-H). Shear zone widening is commonly recognised by increased thickness and decreased deformation intensity in host rock domains. When shear zones affect granitic host rocks, outcrop features like those described for granite mylonites in the Canigó Massif are present (i.e., gneissic aspect including the alignment of biotite crystals) (Fig. 3 and Fig. 4E). Contrarily, when shear zones affect metasedimentary rocks, fine-grained phyllonites composed of quartz and aligned micas are developed (Fig. 4F). SW-NE-oriented brittle fractures (S_f) that postdate all the structures are also present in the Cap de Creus area (Fig. 5).

4.2. Microstructure

At the thin section scale, mylonite belts in the Canigó and Cap de Creus areas show significant variations in mineral phase content,

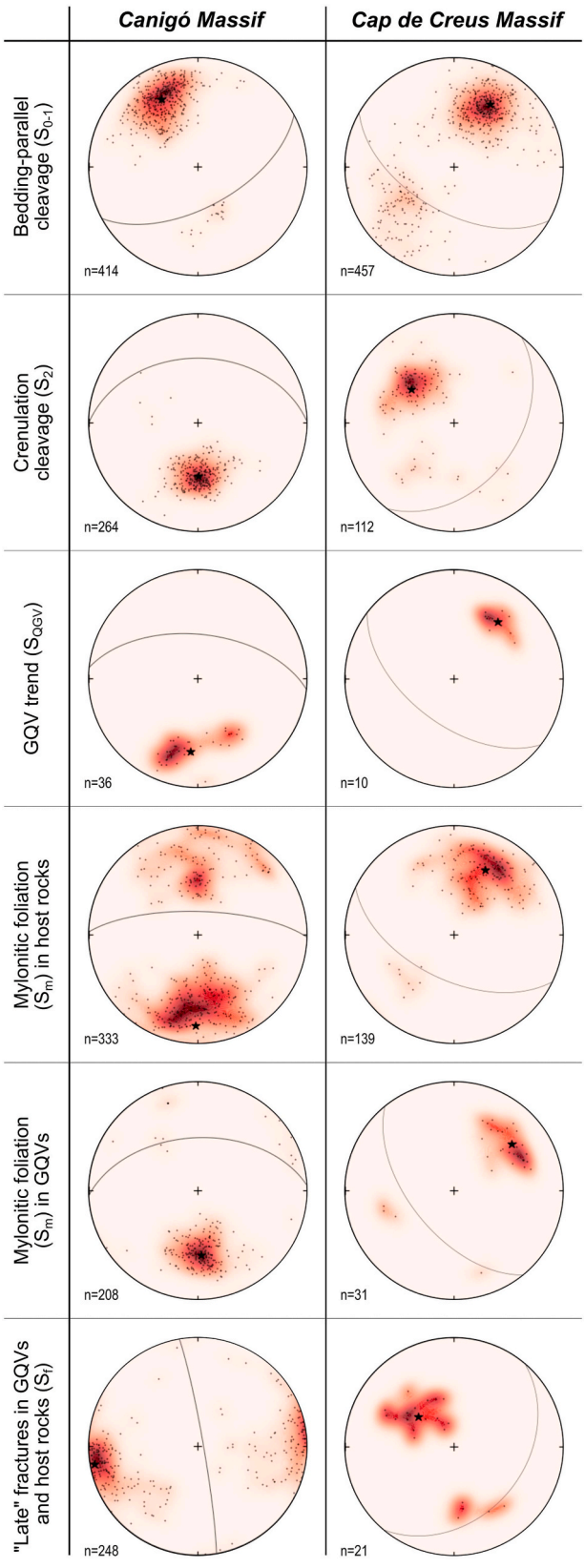

Fig. 5. Equal-area lower hemisphere stereoplots of the main macro- and mesostructures investigated in the Canigó (left) and Cap de Creus (right) Massifs. Note that the S_m and S_{GQV} show a common structural attitude in both areas, and that poles to planes of the S_m are more clustered when they affect GQVs. (For interpretation of the references to colour in this figure legend, the reader is referred to the Web version of this article.)

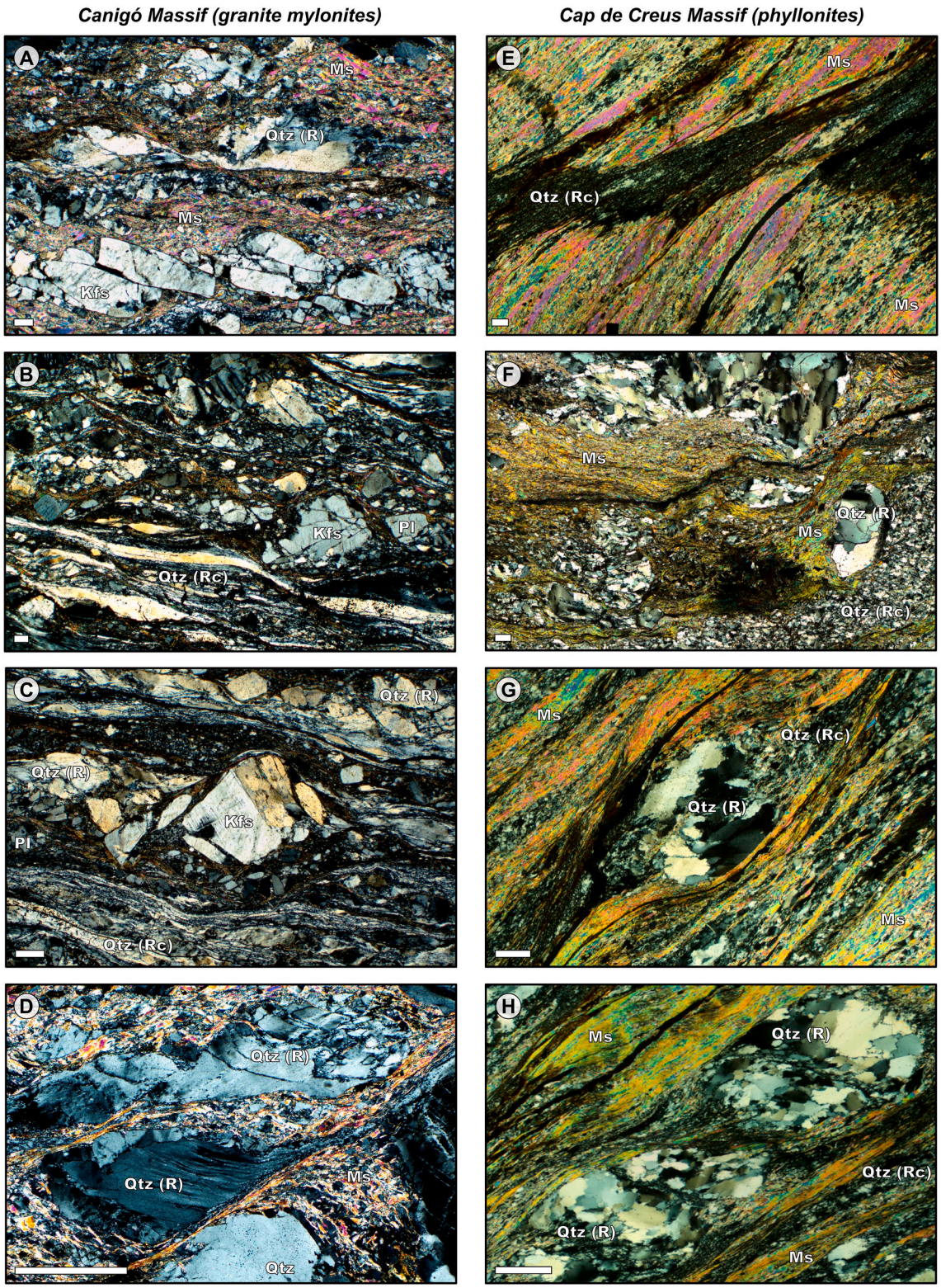

Fig. 6. Microphotographs (crossed polars; XPL) of granitic and metasedimentary host rocks affected by shear zones of the Canigó (A–D) and Cap de Creus (E–F) Massifs, showing relict (R) and recrystallised (Rc) quartz grains. (A) Granite protomylonite where mosaic-fragmented K-feldspar porphyroclasts are embedded in a matrix of muscovite and partially Rc quartz that defines the mylonitic foliation; R quartz crystals are also present. (B, C) Granite mylonite-ultramylonite where quartz is mostly recrystallised and feldspar porphyroclasts exhibit a brittle behaviour. (D) Detail of R quartz crystals with quartz overgrowths in a granite mylonite, which show deformation lamellae and are affected by a micro-shear zone. (E) Phyllonite exhibiting deformation localisation in a micro-shear zone mostly made up by fine-grained Rc quartz. (F–H) Polycrystalline quartz porphyroclasts acting as rigid objects and forming core-mantle structures in a muscovite-rich matrix. Mineral abbreviations following Warr (2021); scalebars are 0.25 mm. (For interpretation of the references to colour in this figure legend, the reader is referred to the Web version of this article.)

revealing significant rheological differences within the host rocks. S_m is well defined at the microscale of the granite mylonites from the Canigó Massif (Fig. 6A–D) by the orientation of muscovite and biotite that forms S-C fabrics (Fig. 6A), the orientation of quartz ribbons, and the elongation of monocrystalline quartz crystals (Fig. 6B and C). Partial recrystallisation of quartz occurs in all the studied samples, whereas K-feldspar crystals behave brittlely forming φ- and σ-type, as well as domino- and mosaic-fragmented porphyroclasts and porphyroclast aggregates (Fig. 6A) (e.g., Passchier and Trouw, 1996). Intracrystalline deformation is also present in the relict quartz grains as lamellae, trails, or veinlets of aligned subgrains, and patchy or chessboard-like undulous extinction (Fig. 6D).

Phyllonites from the Cap de Creus Massif (Fig. 6E–H) show a strong foliation exclusively defined by the orientation of muscovite crystals. S_m bends around polycrystalline quartz porphyroclasts forming S-C fabrics and micro-shear bands that show signs of quartz recrystallisation and grain size reduction at their cores (Fig. 6E). σ-type quartz porphyroclasts show core-and-mantle structures (Fig. 6F–H), in which the core is formed by inequigranular quartz crystals with serrated boundaries and the mantle is composed by fine-grained quartz (± muscovite) aggregates. In some areas, fine-grained recrystallised quartz crystals are the dominant phase of the microstructure (Fig. 6G), although in most cases muscovite crystals with a strong shape preferred orientation represent >90 % of the modal abundance of minerals if quartz porphyroclasts are excluded (Fig. 6E–H).

The quartz mylonites of the two studied areas show similar features at the microscale that reveal quartz dynamic recrystallisation (Fig. 7). Ductile deformation fabrics overprint cataclastic textures in the Canigó Massif (Collada de Roques Blanques area; Fig. 2B), showing inequigranular quartz clasts with strong intracrystalline deformation and a preferred grain elongation (Fig. 7A). Ductile deformation is represented in both areas by protomylonite to ultramylonite areas with S-C fabrics and, in some cases, C' shear bands (Fig. 7B–F). Quartz is dynamically recrystallised through bulging (Fig. 7B and C) and, more often, subgrain rotation (Fig. 7D–F) mechanisms (e.g., Hirth and Tullis, 1992; Stipp et al., 2002). Relict and recrystallised quartz grains sometimes show clear differences in grain size, with relict grains being petrographically distinguishable by their larger size compared to recrystallised ones (Fig. 7D–F). The weak to moderate shape preferred orientations present in the ductile domains (Fig. 7C–F), as well as minor muscovite occurrences (Fig. 7G), define the continuous S_m. Generally, relict quartz grains show patchy undulous extinction and deformation lamellae (Fig. 7B, C, F), as well as trails of subgrains and newly formed grains (Fig. 7F). Quartz mylonites are generally dominated by subgrain rotation recrystallisation both in the Canigó and Cap de Creus Massifs (Fig. 7D–F). However, the quartz mylonites of the Cap de Creus Massif show areas (up to ca. 4 mm^2) where quartz crystals have lobate grain boundaries and amoeboid shapes (Fig. 7G). These areas also show pinning and dragging microstructures and equigranular textures, all of which are interpreted as evidence of grain boundary migration recrystallisation (Fig. 7G). Moreover, quartz aggregates within mylonites of the Cap de Creus Massif sometimes show strain-free, polygonal fabrics with triple junctions at 120°, revealing grain boundary area reduction processes through static recrystallisation (Fig. 7H).

Electron backscatter diffraction (EBSD) analysis of representative mylonite samples from the Canigó and Cap de Creus Massifs provides further information on the CPO evolution during quartz dynamic recrystallisation (Fig. 8). The samples investigated show weak to strong CPOs, as well as different degrees of intra-grain deformation and subgrain formation: quartz grains show a bimodal grain size distribution with large relict grains surrounded by smaller recrystallised grains with homogeneous grain size. The relict grains show higher internal distortion compared to the recrystallised grains and present highly misoriented regions (i.e., subgrains), which have the same size and orientation as the recrystallised grains. The recrystallised grains show low misorientation to the parental grains. These microstructural features are indicative of grain size reduction by subgrain rotation recrystallisation (e.g., Hirth and Tullis, 1992; Stipp et al., 2002) (cf. Fig. 8B and D). Variable CPOs are distributed in ca. 0.3–0.5 mm-thick bands in some cases (Fig. 8B). Grain orientation spread (GOS) values are also highly variable within each sample and allow distinguishing between relict grains (GOS>2.05°) and newly formed grains (recrystallised; GOS<2.05°) (Fig. 8) (Cross et al., 2017). Protomylonite samples are characterised by larger relict grain size, cataclastic overprinting, and by the presence of bulges and minor subgrains (limited by low-angle grain boundaries, LAGB; 2°–10° misorientation) along grain boundaries (Fig. 8A and B). Relict grains in these samples show significant intra-grain deformation as revealed by high grain reference orientation deviation (GROD) values, which are preferentially clustered at grain boundaries and cracks. Mylonite samples *s.s.* (following Sibson, 1977) show moderate to strong CPOs (Fig. 8C–E), significant intra-grain deformation in relict grains (Fig. 8D), and relatively high amounts of subgrains and newly formed grains (>10° misorientation) (Fig. 8C–E).

In the Cap de Creus mylonites, quartz that shows evidence for static recrystallisation is characterised by matrix polygonisation and the partial to complete overprinting of the preexisting fabric (Fig. 7H and Fig. 9). In some cases, larger relict grains are still present within a relatively homogeneous matrix (Fig. 9A), whereas in other cases all grains have the same size and shape, and the scarce relict grains can only be distinguished with the GOS threshold (Fig. 9B). Recrystallised polygonal grains in these samples have a weak CPO, are strain-free, and show minor in-grain misorientations as revealed by low GROD values. In contrast, relict grains show high degrees of internal lattice distortion and host significant amounts of subgrains (Fig. 9).

Pole figures of the samples analysed were constructed to address the CPO evolution during dynamic recrystallisation of the investigated quartz mylonites, as well as the activity of quartz slip systems (Fig. 10, Supplementary Material 3; SM3). Potential differences in the CPO depending on the origin of grains were evaluated by differentiating recrystallised and relict quartz grains following Cross et al. (2017) (GOS threshold of 2.05°; see Fig. 8). Relict quartz grains generally show slightly stronger CPOs, as revealed by a more intense data clustering in the pole figures, independently of the crystallographic direction represented (SM3). However, the pole figures reveal similar fabrics when considering either all grains, or when recrystallised and relict quartz grains are separated. Accordingly, the microstructures investigated are evaluated as one-point-per-grain pole figures including data from all quartz grains in the sample (always above 200 grains per sample) (Fig. 10). Samples show a wide range of quartz c-axis distributions, including asymmetric cross girdles, single girdle, and Y-axis maximum fabrics with moderate to strong CPOs. Noteworthy, weaker fabrics are developed in host rocks (phyllonites and granite mylonites) whereas stronger fabrics are present in quartz mylonites (Fig. 10). The dominant slip systems operating during deformation of the studied samples may be inferred from c-axis distributions in quartz pole figures (see legend in Fig. 10; Schmid and Casey, 1986). Most of the granite mylonite and phyllonite samples have quartz CPOs where the c-axis girdle is perpendicular to the X strain direction, which suggests <a> slip on multiple planes (basal, prism, and rhomb <a> slip, also known as mixed <a> slip; e.g., Barth et al., 2010). One phyllonite sample shows a strong CPO where the c-axis maximum is parallel to the Y strain direction, indicative of dominant prism <a> slip. Quartz mylonites show, in contrast, stronger CPOs with more clustering in the pole figures, which sometimes indicate the exclusive operation of either basal, prism, or rhomb <a> slip. Moreover, samples from the Cap de Creus area that record static grain growth and polygonisation (Fig. 9) show CPOs with a c-axis maxima subparallel to the X strain direction, implying prism <c> slip.

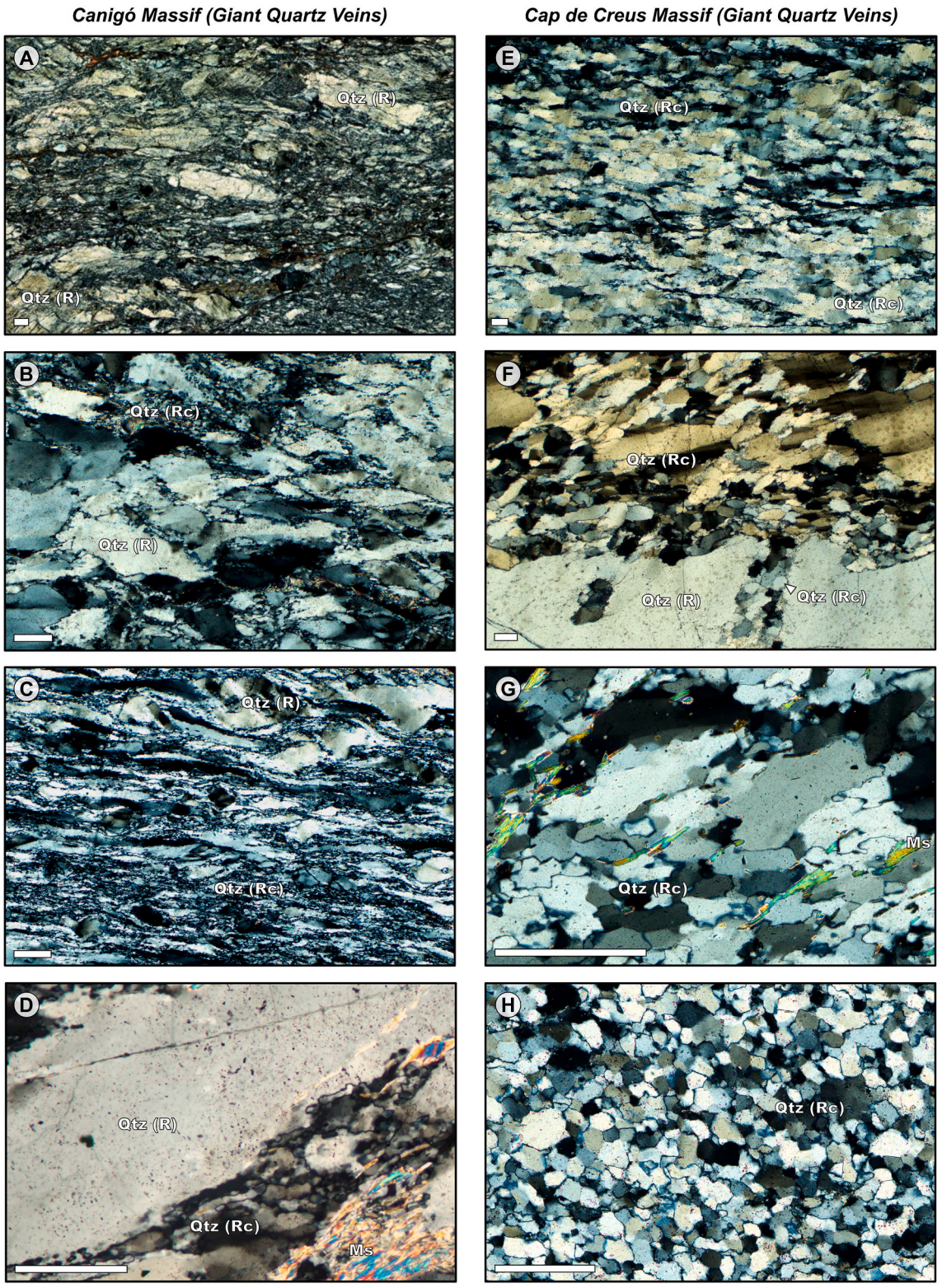

Fig. 7. Microphotographs (crossed polars; XPL) of quartz mylonites (GQVs affected by shear zones) in the Canigó (A–D) and Cap de Creus (E–H) Massifs, showing relict (R) and recrystallised (Rc) quartz grains. (A) Protomylonite showing a ductile deformation fabric overprinting a cataclastic texture. (B, C) Quartz mylonites showing bulging-dominated textures with R and Rc quartz crystals clearly distinguishable on the basis of grain size, developing core-mantle structures. (D–F) Quartz mylonites dominated by subgrain rotation recrystallisation, where a significant amount of Rc grains occur around R grain boundaries showing a shape preferred orientation that defines a continuous mylonitic foliation. (G) Grain boundary migration dominated microstructure with characteristic lobate grain boundaries, amoeboid shapes, and muscovite pining. (H) Polygonal fabric with chiefly equidimensional quartz crystals and triple junctions at ca. 120°, indicative of static recrystallisation. Mineral abbreviations following Warr (2021); scalebars are 0.25 mm. (For interpretation of the references to colour in this figure legend, the reader is referred to the Web version of this article.)

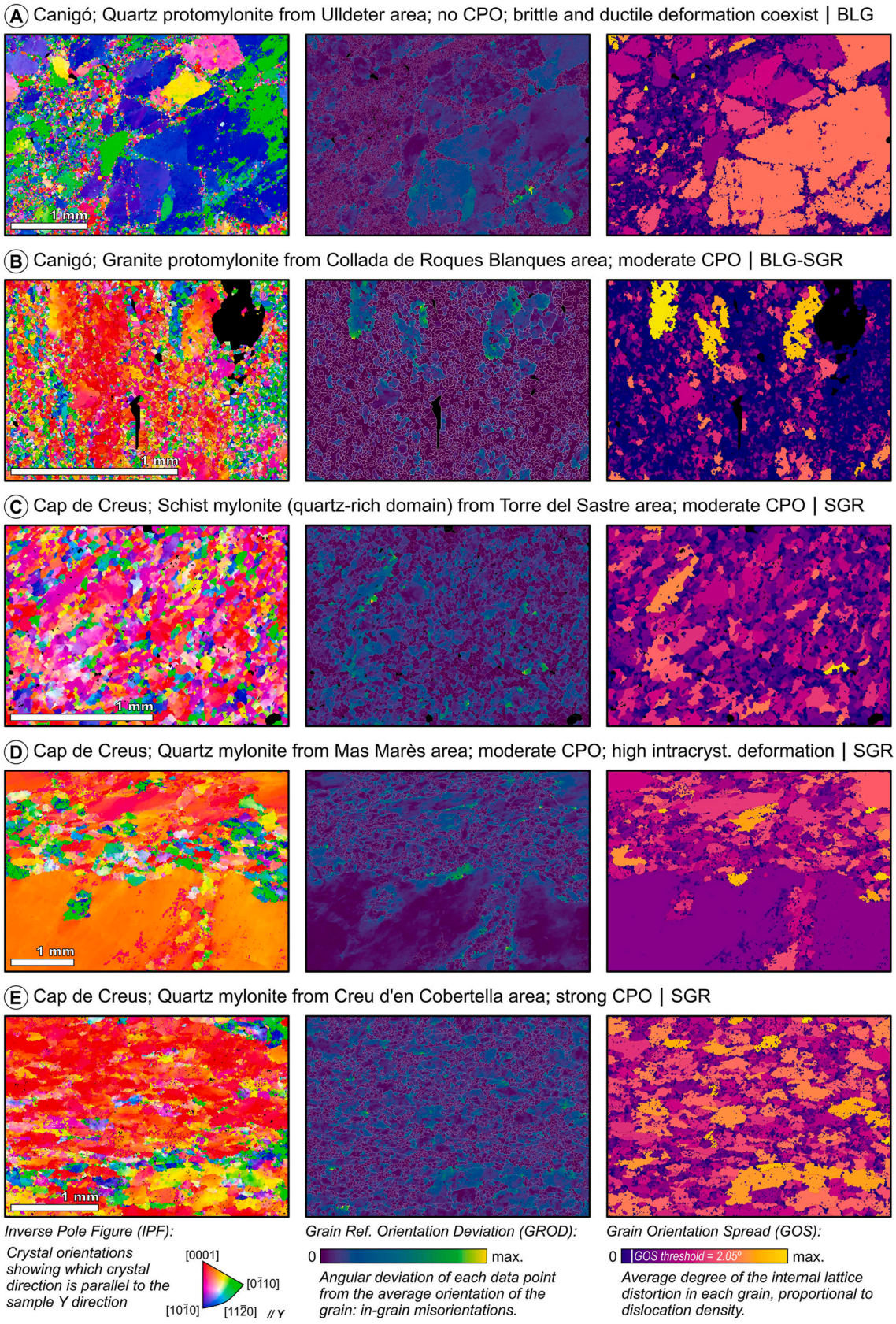

Fig. 8. Inverse pole figure (IPF, left), grain reference orientation deviation (GROD, center), and grain orientation spread (GOS, right) maps obtained through electron backscatter diffraction (EBSD) analyses of quartz and host rock mylonites from the Canigó (A, B) and Cap de Creus (C–E) Massifs. Samples are dominated by bulging recrystallisation (BLG) and subgrain rotation recrystallisation (SGR). Note the two grain size populations that may be correlated with GOS values (right column) above and beneath a 2.05° threshold (relict and recrystallised grains, respectively). See text for further explanations. (For interpretation of the references to colour in this figure legend, the reader is referred to the Web version of this article.)

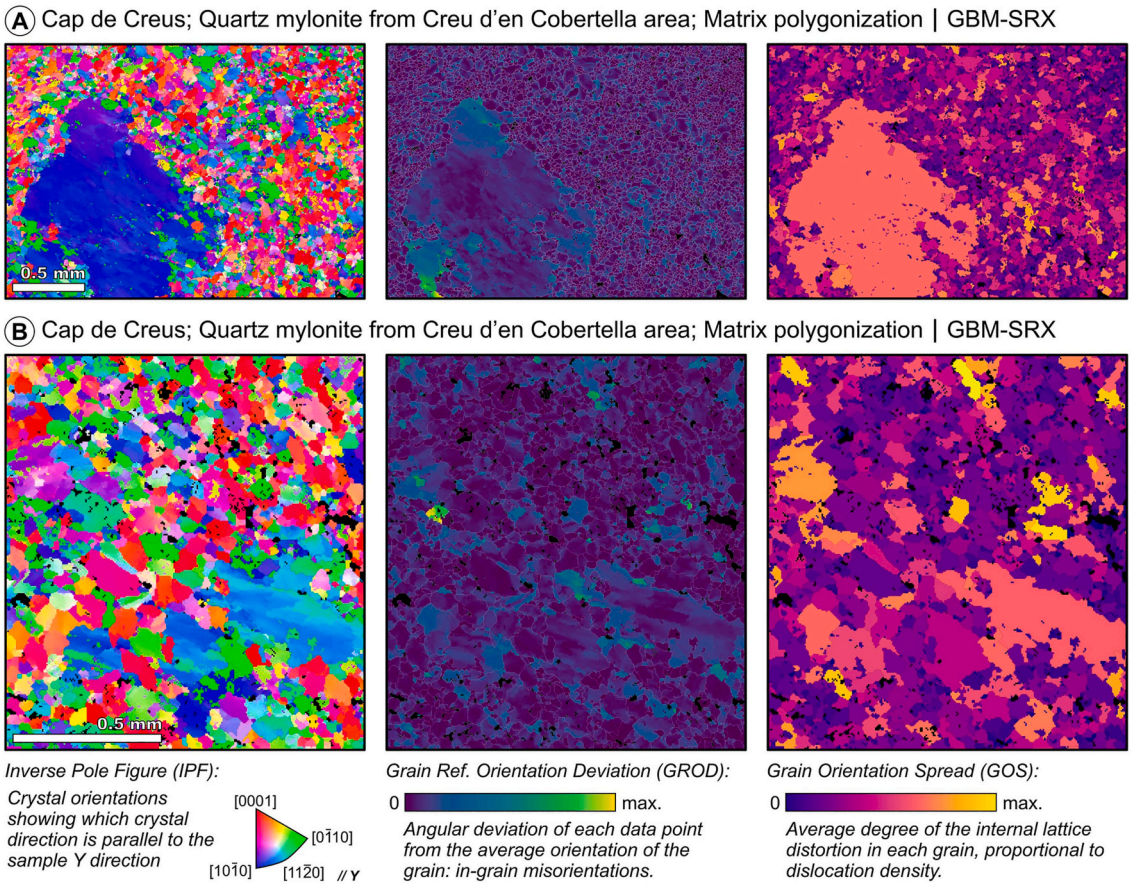

Fig. 9. Inverse pole figure (IPF, left), grain reference orientation deviation (GROD, center), and grain orientation spread (GOS, right) maps obtained through electron backscatter diffraction (EBSD) analyses of quartz mylonites showing grain polygonisation from the Cap de Creus Massif. Samples are dominated by grain boundary migration (GBM) and static recrystallisation (SRX) fabrics. Note that, contrary to the samples in Fig. 8, here there are no relict quartz grains because the pre-existing fabric has been completely overprinted. See main text for further explanations. (For interpretation of the references to colour in this figure legend, the reader is referred to the Web version of this article.)

4.3. Geochronology

The $^{40}Ar/^{39}Ar$ step-heating spectra of apparent ages and corresponding K/Ca ($^{39}Ar_K/^{37}Ar_{Ca}$) for the analysed samples are provided in Fig. 11. The obtained spectra are complex and do not allow a straightforward age determination for the muscovite, since plateau ages, calculated when the ages of at least five consecutive steps covering >50 % of the ^{39}Ar released agree within error, cannot be determined. However, consecutive steps within similar ages covering <50 % of the ^{39}Ar released, often referred to as "pseudo-plateau" or "miniplateau" ages, still contain geologically meaningful information and are often used in the literature (see Schaen et al., 2020). The spectra reflect that all the samples analysed were initially deformed during Pliensbachian-Callovian (164–188 Ma; early-mid Jurassic) times. Noteworthy, analyses carried out in each sampling area show consistent age results. Samples from the Ulldeter area (Fig. 2D) yield younger ages of ca. 164–171 Ma (Fig. 11A and B), whilst those located eastwards, at the Collada de Roques Blanques area (Fig. 2B), initially crystallised at ca. 180–188 Ma (Fig. 11C and D). After the consecutive steps indicating Jurassic initial crystallisation ages, all samples show staircase patterns indicative of K reorganisation and loss of ^{40}Ar. No geochronological information can be extracted from these patterns, although they may indicate different deformation-recrystallisation processes and are thus discussed below. The staircase pattern is continuous until the initial heating steps in two samples (Fig. 11B and C), albeit samples UDT21-09 (Fig. 11A) and RJ21-09 (Fig. 11D) show younger ages of recrystallisation during Aptian-Albian (early Cretaceous) times (ca. 110–118 and 114 Ma, respectively). All samples show relatively constant and generally overlapping K/Ca.

The $^{38}Ar_{Cl}/^{39}Ar_K$ species, as plotted in the Age vs. Cl/K diagrams (Fig. 12), were used to determine whether the analysed muscovite consist of mixed mica populations or recrystallised micas (see Villa et al., 2014; Vissers et al., 2017). All the analysed samples consistently show low (<0.0005) Cl/K values (Fig. 12), even at the first degassing steps when Cl/K are often variable, and only one heating step from the sample RJ21-11A yielded a Cl/K>0.01 (Fig. 12C). This reinforces the reliability of the data because it suggests that: (1) the degassed samples correspond to single muscovite populations, meaning that there is no need of separating the analysed crystals into different grain size fractions, and (2) if the muscovite crystals were recrystallised, the tectonometamorphic conditions of recrystallisation were similar to those during their initial formation.

Zircon U-Pb dating results provided two main age populations at 332 ± 4 Ma and 292 ± 3 Ma (Fig. 13). In cathodoluminescence images, zircons of the older population (~332 Ma) generally correspond to core domains with faint or poorly defined internal zoning, whereas those of the younger population (~292 Ma) occur as rim overgrowths showing more distinct oscillatory zoning. Despite these textural differences, U-Th-Pb contents are homogeneous across both populations (Fig. 13A and B). The early Carboniferous (Visean) age population of 332 ± 4 Ma is significantly older than other age constraints obtained for some of the large granitic plutons throughout the Pyrenees. The early Permian (Sakmarian) zircon age population of 292 ± 3 Ma is slightly younger than the age of the Costabona granodiorite, where the dated dacite

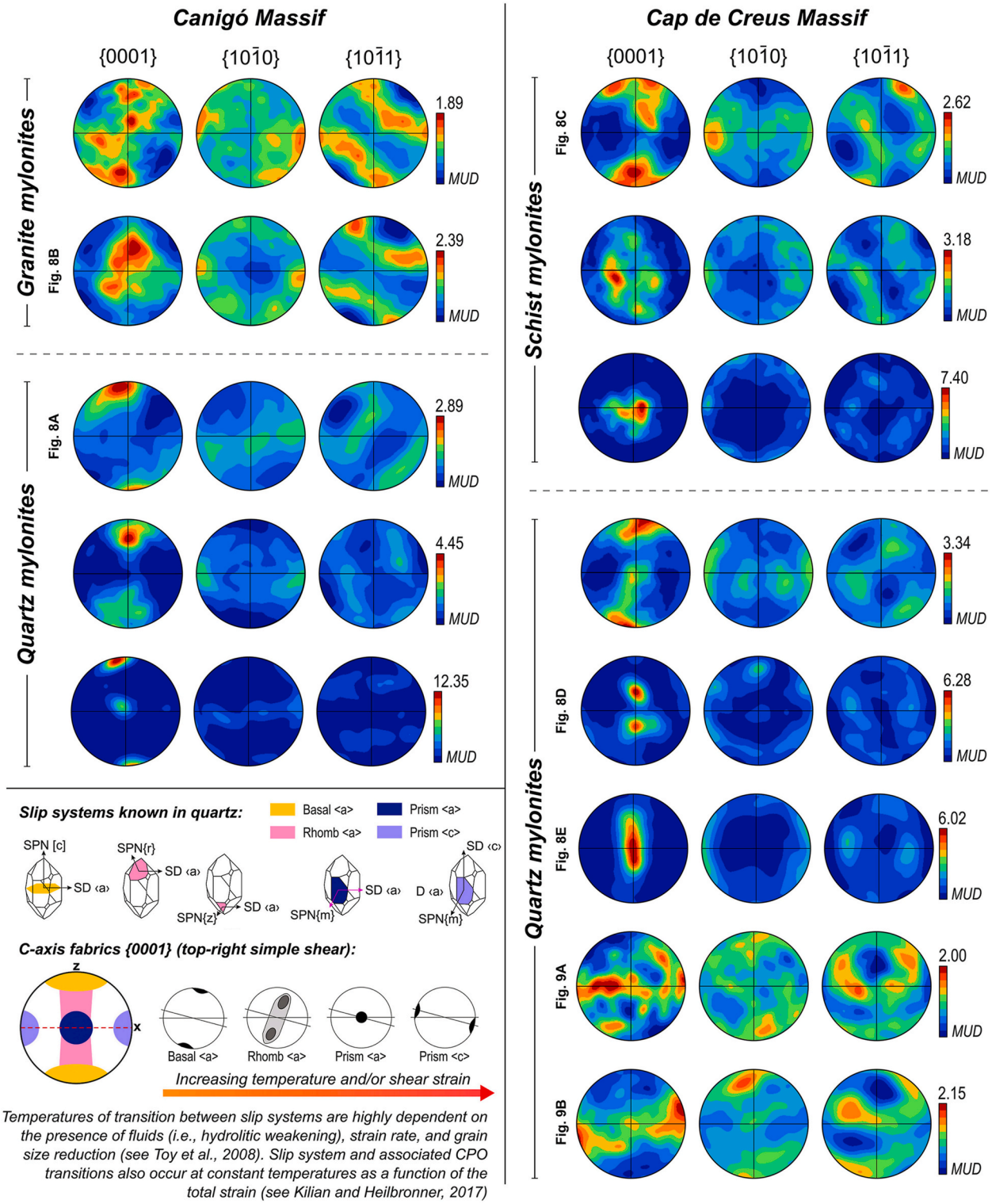

Fig. 10. Quartz crystallographic preferred orientations (CPOs) represented as one-point-per-grain pole figures (lower hemisphere equal-area projections, XZ reference frame; scale units are multiples of uniform density; MUD) parallel to [c], {r}, and {m}, corresponding to {0001}, {10-10}, and {10–11} directions, respectively. Samples are grouped by rock type and correspond to granite and quartz mylonites in the Canigó Massif (left), and to phyllonites (i.e., schist mylonites) and quartz mylonites in the Cap de Creus Massif (right). Quartz mylonites (i.e., deformed GQVs) have stronger CPOs dominated by basal <a>, prism <a>, or prism <c> slip systems, whilst phyllonites and granite mylonites show weaker fabrics mostly dominated by mixed <a> slip. Cartoons of quartz crystals and slip system activity in the legend were adapted from Barth et al. (2010) and Dutta and Mukherjee (2021). See text for further explanations. Note that the colour scale of the MUD, which indicates the intensity of the CPO, is adapted to the values of each sample. (For interpretation of the references to colour in this figure legend, the reader is referred to the Web version of this article.)

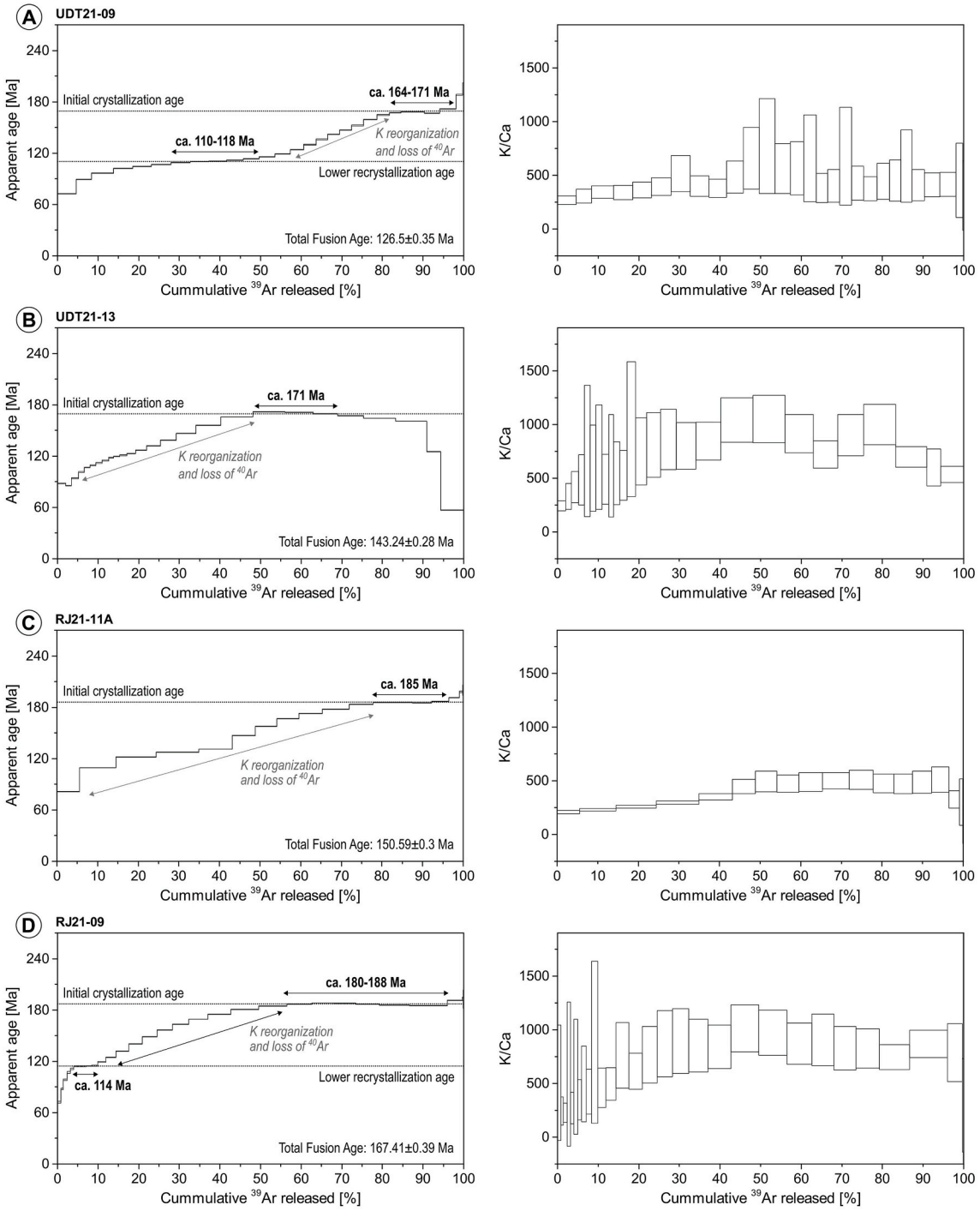

Fig. 11. Apparent age spectra (left) and K/Ca (right) obtained through incremental step-heating $^{40}Ar/^{39}Ar$ dating on muscovite samples found within relatively undeformed domains of GQVs (see raw data in Supplementary Material 1 and sample photos in Supplementary Material 4). Samples are ordered from younger to older initial crystallisation, which occurred during Pliensbachian-Callovian (lower-middle Jurassic) times. Note that spectra (A) and (D) also infer potential lower ages of recrystallisation during Aptian-Albian (lower Cretaceous) times. See text in the discussion for age interpretations.

porphyry dyke is emplaced (302 ± 4 Ma; Laumonier et al., 2015), in agreement with their cross-cutting relationships. Accordingly, it represents the maximum age of GQV formation and shear zone activity, in agreement with the early-mid Jurassic initial crystallisation ages obtained from muscovite $^{40}Ar/^{39}Ar$ age determinations (Fig. 11 and Fig. 12).

5. Discussion

5.1. Shear zone and giant quartz vein age and petrogenesis

The maximum GQV and shear zone formation age of 292 ± 3 Ma (Permian) (Fig. 13C) is the most robust age determination obtained in the present work and agrees with the $^{40}Ar/^{39}Ar$ muscovite initial crystallisation and recrystallisation ages of ca. 164–188 and 110–118 Ma, respectively (Fig. 11). However, $^{40}Ar/^{39}Ar$ step-heating spectra do not allow an unequivocal plateau age calculation. Muscovite degassing

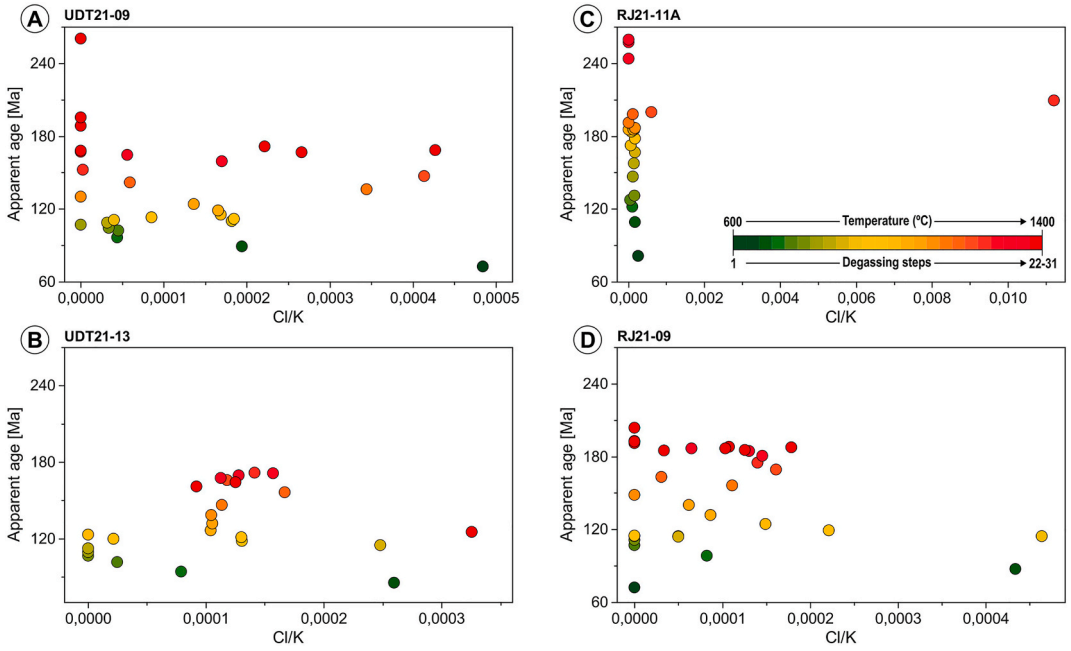

Fig. 12. Age vs. Cl/K diagrams (calculated from the $^{38}Ar_{Cl}/^{39}Ar_K$ species) of the analysed muscovite samples. Colours represent degassing steps (between 22 and 31 depending on sample), which are correlated with increasing temperature from 600 to 1400 °C. Note that all steps from all samples, except for one outlier in (C), show consistently low (<0.0005) Cl/K ratios (cf. Villa et al., 2014; Vissers et al., 2017). See text in the discussion for Cl/K ratios interpretation. (For interpretation of the references to colour in this figure legend, the reader is referred to the Web version of this article.)

patterns indicate K reorganisation and loss of ^{40}Ar postdating initial crystallisation. These patterns have classically been interpreted as proxies indicating either (1) mixed mica populations due to, for example, mica formation in consecutive pulses, (2) the occurrence of thermal events postdating muscovite formation, or (3) prolonged muscovite crystallisation and recrystallisation histories (e.g., Dunlap et al., 1991; Kirschner et al., 1996; Dunlap, 1997; Kula et al., 2010; Bröcker et al., 2013). The low (<0.0005 except for one outlier) values of Cl/K calculated from $^{38}Ar_{Cl}/^{39}Ar_K$ species suggest, however, that the analysed muscovite represent single populations in each sample (see Villa et al., 2014; Vissers et al., 2017) (Fig. 12). Regarding thermal resetting, the known closure temperature of the Ar isotopic system in muscovite ranges, depending on cooling rates and effective diffusion radius, between 350 and 425 °C (Purdy, 1976; Harrison et al., 2009; see a review in Oriolo et al., 2018). According to this, one possible scenario would be that fluids forming the GQVs acted as a heat supply producing this thermal resetting. However, GQVs are affected by the shear zones (Figs. 2–5) and, accordingly, shear zones can at most be coeval, or "late" with respect to GQV formation (see discussion below). Moreover, all primary fluid inclusion assemblages within GQVs, as well as chlorite thermometry calculations, suggest fluid temperatures significantly lower than the known Ar closure temperatures (Ayora and Casas, 1983; Ayora et al., 1984; Fonseca et al., 2015; González-Esvertit et al., 2024). Other thermal events involving temperatures >350 °C and thermal resetting in the analysed samples are also unlikely given the geological evolution of the studied region. For example, time-temperature paths obtained by Maurel et al. (2008) in the Canigó and Montlluís Massifs show systematically decreasing temperatures, always below 300 °C, since upper Cretaceous times.

Alternatively, prolonged crystallisation or successive recrystallisation pulses of the analysed micas, under similar physicochemical conditions, are a more reliable explanation for the complex $^{40}Ar/^{39}Ar$ spectra (Fig. 11) with low and constant Cl/K values (Fig. 12). This scenario allows a qualitative assessment of GQV growth history and shear zone formation (see similar interpretations in Alexandrov et al., 2002; Forster and Lister, 2004; Rolland et al., 2008; Cathelineau et al., 2012; Abd Elmola et al., 2018). Initial Pliensbachian-Callovian crystallisation ages of ca. 164–188 Ma would indicate the onset of mylonitisation in the investigated shear zones, whereas Aptian-Albian (ca. 110–118 Ma) recrystallisation events at temperatures <350 °C and under similar physicochemical conditions may be interpreted as the youngest periods of ductile deformation and shear zone activity. Deformation postdating these events should, however, still be considered when assessing the tectonothermal evolution of the region since early Cretaceous times, although it can be assumed that it occurred at lower temperatures and shallower depths, above the brittle-ductile transition.

After clarifying the Jurassic to early Cretaceous age range for shear zone activity and GQV formation, the analysis of microstructures from representative quartz, mica schist, and granite mylonites provide further insights about how these processes occurred and mutually interacted. The EBSD maps (Fig. 8 and Fig. 9) show that all samples record to some degree dynamic recrystallisation of quartz, evidenced by CPO development and the formation of subgrain boundaries and minor recovery structures. Accordingly, it can be inferred that dislocation creep (grain size insensitive) is the dominant deformation mechanism. Moreover, quartz CPOs and slip systems activity (Fig. 10) are a potentially powerful source of information because they have been suggested to correlate somehow with deformation temperature, degree of flow coaxiality or non-coaxiality, geometry of the kinematic framework, and accumulated strain or strain rate (e.g., Behrmann and Platt, 1982; Schmid and Casey, 1986; Law et al., 1990; Kruhl, 1996; Stipp et al., 2002; Heilbronner and Tullis, 2006; Tokle et al., 2023). These pieces of evidence are based on naturally and experimentally deformed quartzites (Schmid and Casey, 1986; Law, 1987; Mancktelow, 1987; Hirth and Tullis, 1992; Stipp et al., 2002; Toy et al., 2008), as well as in other polymineralic rocks (Menegon et al., 2008; Kilian et al., 2011a, 2011b; Hunter et al., 2016, 2019; Fazio et al., 2017; Casale et al., 2023).

A clear variability of quartz CPO strength and slip system activity may be inferred from the analysed samples, depending on the deformed rock type (Fig. 10). Host rocks (phyllonites and granite mylonites) show weaker fabrics mostly dominated by mixed <a> slip, whereas quartz mylonites have well-defined CPOs where basal <a>, rhomb <a>, and prism <a> and <c> slip systems operate. This fact agrees with macro-structural and textural observations, where strain appears to be higher

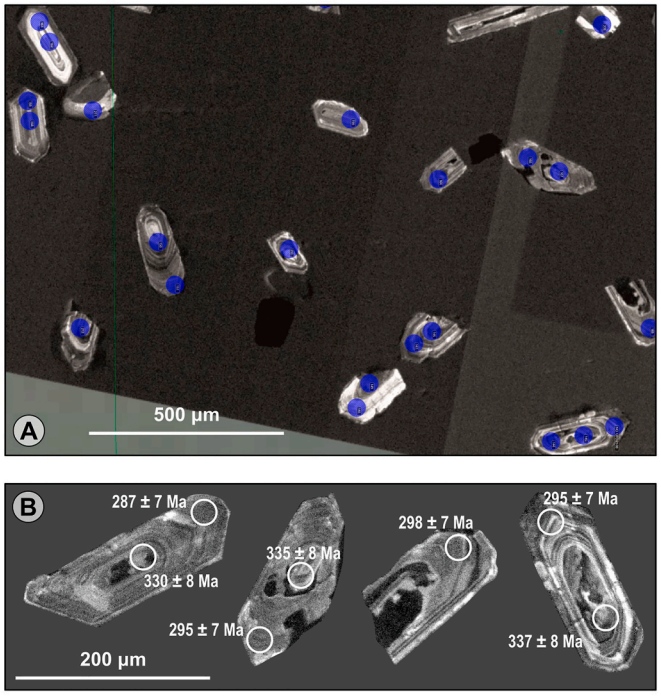

Fig. 13. Cathodoluminescence image of representative zircon grains (A), comparison between core and rim age populations obtained in representative zircon grains (B), and Concordia diagram with the two main age populations of 332 ± 4 Ma and 292 ± 3 Ma (C). Analyses are shown as 2σ uncertainty ellipses and the dark-red numbers correspond to expanded errors also reported throughout the text (i.e., long-term reproducibility; 1 % for zircon). (For interpretation of the references to colour in this figure legend, the reader is referred to the Web version of this article.)

towards the core of deformed GQVs (Fig. 4 and Fig. 7). However, it appears to clash with the scenario expected in this structural-lithological setting, where deformation should be accommodated in the matrix (i.e., by schists and granites) rather than along an elongated rigid object (the GQVs) (e.g., Handy, 1990; Hu et al., 2024). Moreover, the deformation conditions that can be interpreted from the obtained CPOs also seem to be unrealistic, especially when accounting for the deformation temperature. The effects of temperature on the slip system activity are still poorly understood and require careful examination, not only in quartz (e.g., Fig. 8 in Toy et al., 2008; see Fig. 9 in Dutta and Mukherjee, 2021 for an updated compilation) but also in other single- and polyphase aggregates (e.g., Hao et al., 2023). Recently, Kilian and Heilbronner (2017) have demonstrated that the intensification of the Y maximum can occur at constant temperatures with increasing deformation intensity and, therefore, is only function of the total strain. However, it is generally assumed in the literature that quartz cross-girdle fabrics occur at lower temperatures than those dominated by prism <a> and rhomb <a> slip, whereas CPOs with a c-axis maxima subparallel to the X axis of the strain ellipsoid (prism <c> slip) are generally developed at the highest temperatures (Fig. 10). Classical assumptions often relate the activity of mixed <a> slip to high greenschist-amphibolite facies conditions (>400 °C), whilst prism <c> slip is often attributed to eclogite- or granulite-facies temperatures (>550 °C) (Passchier and Trouw, 1996; Barth et al., 2010). However, these temperature assumptions lack solid evidence in naturally deformed rocks. Alternatively, differences in quartz CPOs have also been suggested to result from the combination of oriented growth and dislocation glide (Kilian and Heilbronner, 2017), and not as a result of temperature-dependent activity of different slip systems. Moreover, the temperatures inferred from the obtained CPOs would be much higher than those inferred in the study areas from mineral assemblages, brittle behaviour of K-feldspar (Fig. 6 and Fig. 7), fluid inclusion data, and chlorite thermometry (Ayora and Casas, 1983; Ayora et al., 1984; Fonseca et al., 2015; González-Esvertit et al., 2024). Additionally, one would expect the activation of prism <c> slip with increasing proportion of second phases and a dominance of basal <a> slip in pure quartz domains (e.g., Hippert, 1994; Peternell et al., 2010), rather than the observed patterns, which are exactly the opposite (Fig. 10; SM3). This observation further rules out the possibility that the observed patterns result from the presence or absence of secondary phases or switches in the deformation mechanism.

For all these reasons, a “localising agent” or “strain attractor”, favouring higher strain and enhanced ductility in GQVs than in the surrounding rocks, must be invoked to explain the observed structural-lithological configuration and the apparently contradictory fabrics. One reasonable explanation is the coeval formation and deformation of GQVs, which would involve the presence of a significant amount of water in the rocks being deformed and, therefore, the occurrence of the water-weakening (i.e., hydrolytic weakening) effect (e.g., Blacic, 1975; Blacic and Christie, 1984; Tullis and Yund, 1989; Post and Tullis, 1998). This phenomenon is understood as a strain localisation enhancer because, often, there is a positive correlation between water content and the deformation intensity in sheared rocks. For example, water is believed to accelerate grain boundary migration and grain boundary sliding when present at grain boundaries (Mancktelow and Pennacchioni, 2004), and the water trapped in fluid inclusions of crystals may allow higher rates of diffusion through the crystal lattice (Kronenberg et al., 1990; Post and Tullis, 1998). Moreover, recrystallisation and certain mineral reactions providing free water to the system may also weaken shear zone margins (Oliot et al., 2014), whilst water expelled from shear zones to less deformed rocks can cause further hydrolytic weakening producing widening of high-strain domains in a self-accelerating process (Finch et al., 2016). Accordingly, hydrolytic weakening could have favoured easier dislocation glide due to enhanced ductility in the investigated areas, allowing the activation of slip systems at lower temperatures than those to which they are generally attributed. This would explain the aforementioned inconsistencies on deformation localisation, quartz slip system activities, and temperatures inferred from CPOs (Fig. 10). Furthermore, this would also indicate that GQVs formed over a long-lasting process of continuous or successive pulses of fluid supply and shear zone activity, explaining the complexity of the $^{40}Ar/^{39}Ar$ step-heating spectra that suggest recrystallisation over a time span of >40 Ma (Fig. 11). The strong alteration halos and replacement textures found in the proximity of GQVs and shear zones in these and other areas of the Pyrenees (González-Esvertit et al., 2022a, 2022b, 2025a, 2025b) may also be explained by the occurrence of this phenomenon. In addition to the water-weakening effect, geometrical and mechanical factors related to the orientation of the GQVs relative to the stress field may also have contributed to strain localisation. Quartz veins in the studied areas form very elongate, lens-shaped bodies, composed of

relatively pure quartz. During deformation, if these veins are not perfectly parallel to the shear plane during simple shear, they may have experienced higher stresses due to components of vein-parallel stretching or shortening. This geometric misalignment could result in locally higher strain rates in the quartz bodies compared to the surrounding matrix. Furthermore, the relative quartz purity of the veins may have favoured grain boundary migration recrystallisation over other mechanisms (e.g., Stipp et al., 2002), enhancing the overall ductility of the quartz domains. These effects, in combination with hydrolytic weakening, offer a coherent explanation for the development of high-strain microstructures in the veins and further support their role as strain attractors (see a schematic model of shear zone and GQV genetic relation in Fig. 25 of González-Esvertit, 2025).

5.2. Implications for the structural evolution of the Eastern Pyrenees

The areas investigated in the Cap de Creus and Canigó Massifs are representative of other sectors in the Pyrenees in terms of sedimentation, magmatism, metamorphism, and brittle and ductile deformation (Guitard, 1970; Santanach, 1972a; Den Brok, 1989; Deloule et al., 2002; Casas et al., 2010; Castiñeiras et al., 2011; Aguilar et al., 2014; Navidad et al., 2018; Lemirre et al., 2019; Puddu et al., 2019; Liesa et al., 2021), and they record fingerprints of major geological events reported in other pre-Variscan and Variscan outcrops of SW Europe (Rossi et al., 2009; Casini et al., 2015; Padel et al., 2018; Casas and Murphy, 2018; Álvaro et al., 2018, 2020, 2021; Russo et al., 2022; Casas et al., 2024). Overall, the similarities in terms of geological evolution between the two investigated areas are noteworthy (see stratigraphic correlations between both areas in Castiñeiras et al., 2008; Casas et al., 2010; Navidad et al., 2010, 2018; Martínez et al., 2011; Casas et al., 2019). Neoproterozoic and lower Palaeozoic sediments record similar deformation mesostructures (Figs. 2–5) and low-mid grade metamorphic conditions developed during the Variscan orogeny, although the metamorphic grade increases notably towards the NE in the Cap de Creus Massif (Druguet, 1997). Pre-Variscan magmatism is also represented in both areas (with much larger volumes of magma emplacement in the Canigó Massif; Fig. 1) and is nowadays exposed as granitic orthogneiss outcrops forming the Canigó and El Port orthogneiss bodies (Castiñeiras et al., 2008b, Fig. 1). Moreover, late-Variscan (Carboniferous-Permian) magmatism is exposed as the Costabona monzogranite (ca. 302 ± 4 Ma; Laumonier et al., 2015) and the Roses granodiorite (ca. 290.8 ± 2.9 Ma; Druguet et al., 2014) in the Canigó and Cap de Creus areas, respectively.

Nevertheless, the early Carboniferous (Visean) zircon age population of ca. 332 ± 4 Ma (Fig. 13C) is significantly older than the ages reported for the granitic rocks in the Canigó and Cap de Creus Massifs, as well as older than the widespread late-Variscan magmatism in the Pyrenees (ca. 295–310 Ma) (see an updated summary in Casas et al., 2025). Alternatively, our results support the existence of an early Carboniferous (Visean) magmatic episode in the Pyrenees, in agreement with other zircon ages reported in the central Pyrenees (e.g., Mezger and Gerdes, 2016) and, overall, more akin to the evolution of the whole European Variscides (see review of Casas et al., 2025). The younger zircon age population of ca. 292 ± 3 Ma, in contrast, agrees with the age of the Costabona monzogranite where the sampled dyke is emplaced, as well as with the early-mid Jurassic GQV and shear zone formation $^{40}Ar/^{39}Ar$ ages. The fact that Visean zircons are present within this dyke suggests that both the dyke and Costabona monzogranite could, in part, have originated from the fusion of underlying lower Carboniferous magmatic rocks, nowadays only present as undeformed granite pebbles within the Serpukhovian-Bashkirian Culm conglomerates (Casas et al., 2025).

Postdating these magmatic and tectonometamorphic events, mylonite belts are present in both the Canigó and Cap de Creus areas (Fig. 2 and Fig. 3), as well as in other sectors across the basement rocks of the Pyrenees (Fig. 1 and the references therein). Overall, deformation localisation within these mylonite belts has taken place at all scales, from the regional map (Fig. 2 and Fig. 3) to the outcrop (Fig. 4) and down to the thin section (Fig. 6D, E, H) scale (e.g., Carreras, 2001). The age of these shear zones has been the subject of different interpretations due to a lack of younger magmatic rocks that could provide a minimum deformation age. Accordingly, only a maximum age based on geochronological data, i.e., postdating the late-Variscan magmatic rocks that they deform (Fig. 1), has been established hitherto (e.g., Druguet, 1997; Carreras, 2001; Carreras et al., 2004a; Mezger et al., 2012; Druguet et al., 2014; Laumonier et al., 2015). Zircon U-Pb and muscovite $^{40}Ar/^{39}Ar$ ages reported in this work, however, provide a robust post-Variscan age determination for the mylonite belts cropping out in the Canigó Massif, which can be extrapolated to the Cap de Creus area and to other sectors of the Pyrenees due to the noteworthy resemblance in terms of rock units, structural configuration, and tectonometamorphic evolution (Fig. 1 and Fig. 5). Good examples are the Eocene crystallisation ages of synkinematic micas (ca. 44–38 Ma) recently reported by Monié et al. (2025), or the middle Jurassic ages obtained by Vissers et al. (2017), for the shear zones in the Cap de Creus Massif. These latter age determinations, very similar to those obtained in this work, were interpreted as related to the rifting of the Piemonte-Ligurian Ocean separating the Iberia and Adria plates. Evidence of this rifting period is well documented in different regions of SW Europe. In the Pyrenees, it resulted in NNE-SSW-directed extension from late Jurassic to mid Cretaceous times (Vissers et al., 2013; Tavani et al., 2018), although evidence for this event has rarely been reported in the basement rocks. Present-day orientations of the investigated mylonite belts (Figs. 1–3, Fig. 5) are, however, in agreement with this rifting extension direction (cf. Vissers et al., 2017). Moreover, Pitra and Martínez (2024) also suggested a similar age for fluid circulation events leading to kyanite-, staurolite-, and chloritoid-bearing pseudomorphs in the northern area of the Cap de Creus Massif, whereas Laumonier et al. (2015) also acknowledged the possibility that GQVs affected by shear zones in the Canigó Massif were formed during Jurassic times. In fact, mylonite bands in the northern sector of the Canigó Massif are difficult to reconcile with Variscan times, since they bring Cambrian-Ordovician rocks over Triassic ones (Guitard, 1965, 1970; Margalef et al., 2023). Based on regional comparisons, there is also difficulty fitting formation temperatures of GQVs in other sectors of the Pyrenees (<200 °C in the La Cerdanya area) within the Variscan tectonothermal evolution of the orogen (González-Esvertit et al., 2024), as well as with the late-Variscan age of the dacite porphyry dyke dated in the present work. All these works, as well as the shear zone and GQV ages presented here, contradict classical assumptions stating that the Pyrenean mylonite belts and associated GQVs developed during the retrograde stages of the Variscan orogeny, which are not supported by geochronological data (Carreras et al., 1980; Bons et al., 2004; Druguet and Carreras, 2019). Accordingly, we suggest that the structural evolution of this region during Jurassic times should be investigated in more detail from a geochronological approach, rather than proceeding with the classical assumption that ductile deformation in the Pyrenees was exclusively developed during the Variscan orogeny.

Given the spatial distribution of samples, the location and deformation propagation direction of the mylonite belts in the Canigó Massif can also be addressed. Samples showing oldest initial crystallisation ages (ca. 180–188 Ma) correspond to the easternmost sector of the study area (Collada de Roques Blanques area; Fig. 2B), whilst samples with younger ages (ca. 164–171 Ma) were taken ca. 10 km westwards and at a similar structural altitude (Ulldeter area; Fig. 2D) (Fig. 5 and Fig. 11). This suggests that deformation along the main mylonitic band of the study area (Fig. 2A) may have propagated westwards during at least ca. 10 m.y. of shear zone activity. Despite representing a significant time span, similar or longer shear zone longevities have already been reported in other sectors (e.g., Schneider et al., 2013; Beaudoin et al., 2020). In contrast, younger recrystallisation ages overlap in both areas at ca. 110–118 Ma (Fig. 11). Other investigations on mylonites from the Canigó Massif are scarce and restricted to the works of Casas (1982, 1986). In these contributions, microstructural descriptions and quartz

c-axis fabric distributions are evaluated in shear zones affecting GQVs and the Costabona monzogranite, and it is suggested that deformation took place under low-temperature conditions. Moreover, the similarity of the studied microstructures with those found in well-foliated mylonites deformed under higher-temperature conditions is also highlighted (Casas, 1982, 1986).

Overall, the two investigated massifs could be representative, in terms of age and formation processes, of other sectors in the Pyrenees where GQVs are also associated with mylonite bands and strong fluid-rock alterations in the host rocks (see a GIS compilation of more than 700 GQVs in the GIVEPY database, https://givepy.info; González-Esvertit et al., 2022a). It is worth noting that not all the GQVs in the basement of the Pyrenees record mylonitic fabric development. Those that are not associated with mylonite belts are, in turn, the GQVs that show lowest dipping angles (ca. 20–50°) and have been associated with Alpine thrust activity (González-Esvertit et al., 2023). Accordingly, the GQV formation ages provided in this work cannot be extrapolated to all the GQVs in the Pyrenees, but at most to those showing similar structural features (i.e., steep or subvertical dips and genetically associated with mylonite belts). In this framework, the relationship between GQV formation and shear zone reactivation, thrust activity, and seismogenic faulting during the Alpine orogeny, since late Cretaceous times, also deserves future attention (McCaig and Miller, 1986; Soula et al., 1986; Majoor, 1988; Monie et al., 1994; Maurel, 2003; Vissers et al., 2020).

6. Conclusions

This study evaluates the age and petrogenesis of mylonite belts and associated Giant Quartz Veins (GQVs) across different scales in the basement rocks of the Pyrenees (SW Europe). Four consistent $^{40}Ar/^{39}Ar$ degassing spectra, obtained from single syn-kinematic muscovite populations found in quartz mylonites, yield initial crystallisation ages of ca. 164–188 Ma. Lower recrystallisation ages of ca. 110–118 Ma have also been obtained for two samples and indicate the youngest period of ductile deformation and shear zone activity. These results agree with a maximum GQV and shear zone age of ca. 292 ± 3 Ma obtained through U-Pb analysis in zircons from a dacite porphyry dyke, which also suggests the presence of an early Carboniferous (ca. 332 ± 4 Ma; Visean) magmatic episode in the Pyrenees. The results reveal that mylonite belts and associated GQVs developed during Jurassic to early Cretaceous times in the Canigó Massif. This agrees with an increasing number of datasets that challenge classical attributions of shear zone formation to the retrograde stages of the Variscan orogeny at other sectors of the Pyrenean basement. The similarity between the Canigó and Cap de Creus Massifs with other surrounding areas in terms of rock types, magmatism, metamorphism, and brittle and ductile deformation events allow us to discuss how representative these data are in the broader context of the Eastern Pyrenees and SW Europe. Finally, we highlight that the structural evolution of the basement rocks in the Pyrenees during Mesozoic (mainly Jurassic) times deserves further attention.

A qualitative assessment of shear zone and GQV growth history is further provided by macro-, meso-, and microstructural evaluation of the study areas, coupled to the $^{40}Ar/^{39}Ar$ degassing spectra interpretation and crystallographic preferred orientation analysis of quartz on various sheared rock types. Discrepancies on the strain distribution, quartz slip systems activity, and temperatures of deformation allow suggesting that GQV formation and mylonitisation were coupled, coeval and long-lasting during successive or continuous pulses of fluid supply and shear zone activity, from early Jurassic to early Cretaceous times. Hydrolytic weakening caused by coeval formation and deformation of GQVs is invoked as a "localising agent" or "strain attractor", which enabled easier dislocation glide and creep in quartz-rich domains allowing strain localisation and transitions between slip systems at lower temperatures due to enhanced ductility when compared to surrounding polymineralic rocks. These results have implications for the current knowledge of deformation localisation and shear zone initiation in crystalline rocks, as well as for the formation mechanisms of GQVs associated with shear zones in other tectonic settings.

CRediT authorship contribution statement

Eloi González-Esvertit: Writing – original draft, Software, Resources, Methodology, Investigation, Formal analysis, Data curation, Conceptualization. **Josep Maria Casas:** Writing – review & editing, Validation, Supervision, Resources, Investigation, Formal analysis, Conceptualization. **Àngels Canals:** Writing – review & editing, Validation, Supervision, Investigation, Formal analysis, Conceptualization. **Paul D. Bons:** Writing – review & editing, Validation, Supervision, Investigation, Formal analysis. **Kevin Konrad:** Writing – review & editing, Validation, Methodology, Data curation. **Maria-Gema Llorens:** Writing – review & editing, Supervision, Methodology, Formal analysis, Data curation. **Gabriel Serrano-López:** Writing – review & editing, Validation, Methodology, Formal analysis. **Claudia Prieto-Torrell:** Writing – review & editing, Visualization, Validation, Methodology, Conceptualization. **Joyce Neilson:** Writing – review & editing, Validation, Resources, Methodology, Formal analysis. **Diego Domínguez-Carretero:** Writing – review & editing, Methodology. **Aratz Beranoaguirre:** Writing – review & editing, Resources, Methodology, Investigation. **Axel Gerdes:** Writing – review & editing, Resources, Methodology, Formal analysis. **Enrique Gomez-Rivas:** Writing – review & editing, Validation, Supervision, Resources, Methodology, Investigation, Conceptualization.

Declaration of competing interest

The authors declare that they have no known competing financial interests or personal relationships that could have appeared to influence the work reported in this paper.

Acknowledgements

We sincerely thank Editor Virginia Toy and two anonymous referees for their valuable comments and suggestions, Carles Ayora for his help during fieldwork at the Esquerdes de Rojà area, and John Still for his assistance with SEM-EBSD data acquisition at the ACEMAC Facility (University of Aberdeen). We acknowledge Oxford Instruments for providing a Student Licence of the AZtecFlex software package. This research was funded by the DGICYT Projects PID2020-118999GBI00, PID2021-122467NB-C22, PID2021-125585NB-I00, and PID2022-139943NB-I00 (MCIN/AEI/FEDER-UE/10.13039/501100011033), CNS2023-145382 (MCIN/AEI/10.13039/501100011033/EUNextGenerationEU/PRT), the "Modelitzacio Geodinamica de la Litosfera" (Generalitat de Catalunya, 2021 SGR 00410), "Sedimentary Geology" (Generalitat de Catalunya, 2021 SGR 00349) and "GEOXiS" (Generalitat de Catalunya, 2021 SGR 00262) Consolidated Research Groups, and the VolcPeG Research Group. EGE acknowledges the funding provided by the Geological Society of London (GSL) Student Research Grants and the PhD grants funded by Generalitat de Catalunya and the European Social Fund (2021 FI_B 00165 and 2022 FI_B1 00043). CPT acknowledges the PhD grant 2021 FISDU 00347 funded by Generalitat de Catalunya. FIERCE is financially supported by the Deutsche Forschungsgemeinschaft (DFG: INST 161/921-1 FUGG, INST 161/923-1 FUGG and INST 161/1073-1 FUGG), and received financial support from the Wilhelm and Else Heraeus Foundation, which is gratefully acknowledged. This is FIERCE contribution No. 220.

Appendix A. Supplementary data

Supplementary data to this article can be found online at https://doi.org/10.1016/j.jsg.2025.105584.

Data availability

Data is available in the Supplementary Materials

References

Abd Elmola, A., Buatier, M., Monié, P., Labaume, P., Trap, P., Charpentier, D., 2018. 40Ar/39Ar muscovite dating of thrust activity: a case study from the Axial zone of the pyrenees. Tectonophysics 745, 412–429. https://doi.org/10.1016/j.tecto.2018.09.004.

Adams, F.D., 1901. The excursion to the pyrenees in connection with the eighth international geological congress. J. Geol. 9, 28–46. https://doi.org/10.1086/620878.

Aguilar, C., Liesa, M., Castiñeiras, P., Navidad, M., 2014. Late Variscan metamorphic and magmatic evolution in the eastern pyrenees revealed by U–Pb age zircon dating. J. Geol. Soc. 171, 181–192. https://doi.org/10.1144/jgs2012-086.

Aiglsperger, T., Proenza, J.A., Zaccarini, F., Lewis, J.F., Garuti, G., Labrador, M., Longo, F., 2015. Platinum group minerals (PGM) in the falcondo Ni-laterite deposit, Loma caribe peridotite (dominican republic). Miner. Deposita 50, 105–123. https://doi.org/10.1007/s00126-014-0520-9.

Alexandrov, P., Ruffet, G., Cheilletz, A., 2002. Muscovite recrystallization and saddle-shaped 40Ar/39Ar age spectra: example from the blond granite (Massif Central, France). Geochem. Cosmochim. Acta 66, 1793–1807. https://doi.org/10.1016/S0016-7037(01)00895-X.

Álvaro, J.J., Casas, J.M., Clausen, S., Quesada, C., 2018. Early Palaeozoic geodynamics in NW Gondwana. J. Iber. Geol. 44, 551–565. https://doi.org/10.1007/s41513-018-0079-x.

Álvaro, J.J., Casas, J.M., Quesada, C., 2021. Reconstructing the Pre-variscan Puzzle of Cambro-Ordovician Basement Rocks in the Southwestern European Margin of Gondwana, 503. Geological Society, London, Special Publications, pp. 531–562. https://doi.org/10.1144/SP503-2020-89.

Álvaro, J.J., Sánchez-García, T., Puddu, C., Casas, J.M., Díez-Montes, A., Liesa, M., Oggiano, G., 2020. Comparative geochemical study on Furongian–earliest Ordovician (Toledanian) and Ordovician (Sardic) felsic magmatic events in south-western Europe: underplating of hot mafic magmas linked to the opening of the Rheic Ocean. Solid Earth 11, 2377–2409. https://doi.org/10.5194/se-11-2377-2020.

Auréjac, J.-B., Gleizes, G., Diot, H., Bouchez, J.-L., 2004. The Quérigut Complex (Pyrenees, France) revisited by the AMS technique : a syntectonic pluton of the Variscan dextral transpression. Bull. Soc. Geol. Fr. 175, 157–174. https://doi.org/10.2113/175.2.157.

Autran, A., Fonteilles, M., Guitard, G., 1970. Relations entre les intrusions de granitoides, l'anatexie, et le métamorphisme regional considertes principalment du point de vue de l'eau: cas de la Chaine Hercynienne des Pyrénées Orientales: ercynienne des Pyrénées Orientales. Bull. Soc. Géol. de France 7 (4), 673–731.

Autran, A., Guitard, G., 1968. Carte géologique détaillée de la France à 1/80.000: prades. BRGM, v. Service de la Carte Géologique de France.

Ayora, C., Carreras, J., Casas, J.M., Liesa, M., 1984. Informe Quarsos. Internal Report of the University of Barcelona (Available Under Request). Barcelona, Universitat De Barcelona.

Ayora, C., Casas, J.M., 1983. Estudi microtermomètric dels filons de quars de les Esquerdes de Rojà, Massís de Canigó, Pirineu Oriental. Acta Geol. Hisp. 18, 35–46.

Balbas, A., Jung, C., Konrad, K., 2023. The origin of the Musicians Seamount Province and its inferences for Late Cretaceous Pacific Plate Motion. Mar. Geol. 465, 107166. https://doi.org/10.1016/j.margeo.2023.107166.

Barrón, P., 2023. La estructura del paleozoico en el valle de soulcem (zona axial, pirineos franceses): la terminación occidental de la falla de merens. Trab. Geol. 11–35.

Barth, N.C., Hacker, B.R., Seward, G.G.E., Walsh, E.O., Young, D., Johnston, S., 2010. Strain Within the ultrahigh-pressure Western Gneiss Region of Norway Recorded by Quartz Cpos, 335. Geological Society, London, Special Publications, pp. 663–685. https://doi.org/10.1144/SP335.27.

Beaudoin, A., Scaillet, S., Mora, N., Jolivet, L., Augier, R., 2020. In situ and step-heating 40Ar/39Ar dating of white Mica in low-temperature shear zones (Tenda massif, Alpine Corsica, France). Tectonics 39, e2020TC006246. https://doi.org/10.1029/2020TC006246.

Behrmann, J.H., Platt, J.P., 1982. Sense of nappe emplacement from quartz c-axis fabrics; an example from the Betic Cordilleras (Spain). Earth Planet Sci. Lett. 59, 208–215.

Beranoaguirre, A., Vasiliev, I., Gerdes, A., 2022. In situ LA-ICPMS U–Pb dating of sulfates: applicability of carbonate reference materials as matrix-matched standards. Geochronology 4, 601–616. https://doi.org/10.5194/gchron-4-601-2022.

Blacic, J.D., 1975. Plastic-deformati on mechanisms in quartz: the effect of water. Tectonophysics 27, 271–294. https://doi.org/10.1016/0040-1951(75)90021-9.

Blacic, J.D., Christie, J.M., 1984. Plasticity and hydrolytic weakening of quartz single crystals. J. Geophys. Res. Solid Earth 89, 4223–4239. https://doi.org/10.1029/JB089iB06p04223.

Bons, P.D., et al., 2004. Apparent boudinage in dykes. J. Struct. Geol. 26 (4), 625–636.

Bons, P.D., et al., 2016. Converging flow and anisotropy cause large-scale folding in Greenland's ice sheet. Nat. Commun. 7, 11427. https://doi.org/10.1038/ncomms11427.

Bröcker, M., Baldwin, S., Arkudas, R., 2013. The geological significance of 40Ar/39Ar and Rb–Sr white mica ages from Syros and Sifnos, Greece: a record of continuous (re) crystallization during exhumation? J. Metamorph. Geol. 31, 629–646. https://doi.org/10.1111/jmg.12037.

Bürgmann, R., Dresen, G., 2008. Rheology of the lower crust and upper mantle: evidence from rock mechanics, geodesy, and field observations. Annu. Rev. Earth Planet Sci. 36, 531–567. https://doi.org/10.1146/annurev.earth.36.031207.124326.

Caldera, N., Teixell, A., Griera, A., Labaume, P., Guardia, M., 2023. Alpine ductile deformation of the upper iberian collided Margin (Eaux-Chaudes massif, West-Central pyrenean hinterland, France). Tectonics 42, e2023TC007828. https://doi.org/10.1029/2023TC007828.

Cao, S., Neubauer, F., 2016. Deep crustal expressions of exhumed strike-slip fault systems: shear zone initiation on rheological boundaries. Earth Sci. Rev. 162, 155–176. https://doi.org/10.1016/j.earscirev.2016.09.010.

Carreras, J., 2001. Zooming on Northern Cap de Creus shear zones. J. Struct. Geol. 23, 1457–1486. https://doi.org/10.1016/S0191-8141(01)00011-6.

Carreras, J., Capella, I., 1994. Tectonic levels in the Palaeozoic basement of the Pyrenees: a review and a new interpretation. J. Struct. Geol. 16, 1509–1524. https://doi.org/10.1016/0191-8141(94)90029-9.

Carreras, J., Casas, J.M., 1987. On folding and shear zone-development: a mesoscale structural study on the transition between two different tectonic styles. Tectonophysics 135, 87–98. https://doi.org/10.1016/0040-1951(87)90154-5.

Carreras, J., Cirés, J., 1986. The geological significance of the western termination of the Mérens Fault at Port Vell (central Pyrenees). Tectonophysics 129, 99–114. https://doi.org/10.1016/0040-1951(86)90248-9.

Carreras, J., Druguet, E., Griera, A., Soldevila, J., 2004a. Strain and Deformation History in a Syntectonic Pluton. the Case of the Roses Granodiorite (Cap De Creus, Eastern Pyrenees), 224. Geological Society, London, Special Publications, pp. 307–319. https://doi.org/10.1144/GSL.SP.2004.224.01.19.

Carreras, J., Druguet, E., Griera, A., Soldevila, J., 2004b. Strain and Deformation History in a Syntectonic Pluton. the Case of the Roses Granodiorite (Cap De Creus, Eastern Pyrenees), 224. Geological Society, London, Special Publications, pp. 307–319. https://doi.org/10.1144/GSL.SP.2004.224.01.19.

Carreras, J., Julivert, M., Santanach, P., 1980. Hercynian myionite belts in the eastern Pyrenees: an example of shear zones associated with late folding. J. Struct. Geol. 2, 5–9.

Carreras, J., Losantos, M., 1982. Geological Setting of the Roses Gtanodiorite (E-Pyrenees, Spain), 4. Acta Geologica Hispanica, pp. 211–217.

Casale, G., Levine, J.S.F., Economou, J., 2023. Extracting quartz deformation fabrics from polymineralic rocks. J. Struct. Geol. 173, 104893. https://doi.org/10.1016/j.jsg.2023.104893.

Casas, J.M., 1984. Estudi De La Deformació En Els Gneis Del Massís Del Canigó: Phd Thesis. Universitat de Barcelona, Barcelona unpublished, 284pp.

Casas, J.M., 2010. Ordovician deformations in the Pyrenees: new insights into the significance of Pre-Variscan ('sardic') tectonics. Geol. Mag. 147, 674–689. https://doi.org/10.1017/S0016756809990756.

Casas, J.M., 1982. Pseudo-two-girdles c-axis fabric patterns in a quartz-feldspar mylonite (Costabona granodiorite, Canigó massif). Acta Geol. Hisp. 17, 151–157.

Casas, J.-M., 1986. Shear bands and related extensional structures in a mylonitized quartz dyke. J. Struct. Geol. 8, 693–699. https://doi.org/10.1016/0191-8141(86)90074-X.

Casas, J.M., Álvaro, J.J., Clausen, S., Padel, M., Puddu, C., Sanz-López, J., Sánchez-García, T., Navidad, M., Castiñeiras, P., Liesa, M., 2019. Palaeozoic basement of the pyrenees. In: Quesada, C., Oliveira, J.T. (Eds.), The Geology of Iberia: a Geodynamic Approach. Springer International Publishing, Regional Geology Reviews, Cham, pp. 229–259. https://doi.org/10.1007/978-3-030-10519-8_8.

Casas, J.M., Brendan Murphy, J., 2018. Unfolding the arc: the use of pre-orogenic constraints to assess the evolution of the Variscan belt in Western Europe. Tectonophysics 736, 47–61. https://doi.org/10.1016/j.tecto.2018.04.012.

Casas, J.M., Castiñeiras, P., Navidad, M., Liesa, M., Carreras, J., 2010. New insights into the late Ordovician magmatism in the Eastern Pyrenees: U–Pb SHRIMP zircon data from the Canigó massif. Gondwana Res. 17, 317–324. https://doi.org/10.1016/j.gr.2009.10.006.

Casas, J.M., González-Esvertit, E., Beranoaguirre, A., Domínguez-Carretero, D., Canals, À., Gomez-Rivas, E., Margalef, A., Figueras, F., Gerdes, A., 2025. U-Pb-age from undeformed granite pebbles in Carboniferous Culm conglomerates: new geochronological constrains on the Variscan events in the Pyrenees. Lithos 516–517, 108227. https://doi.org/10.1016/j.lithos.2025.108227.

Casas, J.M., Navidad, M., Castiñeiras, P., Liesa, M., Aguilar, C., Carreras, J., Hofmann, M., Gärtner, A., Linnemann, U., 2015. The Late Neoproterozoic magmatism in the Ediacaran series of the Eastern pyrenees: new ages and isotope geochemistry. Int. J. Earth Sci. 104, 909–925. https://doi.org/10.1007/s00531-014-1127-1.

Casas, J.M., Sánchez-García, T., Díez-Montes, A., Clariana, P., Margalef, A., Valverde-Vaquero, P., Beranoaguirre, A., Román-Alpiste, M.J., Pujol-Solà, N., Álvaro, J.J., 2024. Extent and Significance of the Upper Ordovician Felsic Volcanism in the Pyrenees and Mouthoumet Massifs, SW Europe, 542. Geological Society, London, Special Publications, pp. 2022–2358. https://doi.org/10.1144/SP542-2022-358. SP542.

Casini, L., Cuccuru, S., Maino, M., Oggiano, G., Puccini, A., Rossi, P., 2015. Structural map of Variscan northern Sardinia (Italy). J. Maps 11, 75–84. https://doi.org/10.1080/17445647.2014.936914.

Castiñeiras, P., Navidad, M., Casas, J.M., Liesa, M., Carreras, J., 2011. Petrogenesis of Ordovician magmatism in the pyrenees (Albera and canigó Massifs) determined on the basis of Zircon minor and trace element composition. J. Geol. 119, 521–534. https://doi.org/10.1086/660889.

Castiñeiras, P., Navidad, M., Liesa, M., Carreras, J., Casas, J.M., 2008a. U–Pb zircon ages (SHRIMP) for Cadomian and early Ordovician magmatism in the Eastern Pyrenees: new insights into the Pre-Variscan evolution of the northern Gondwana margin. Tectonophysics 461, 228–239. https://doi.org/10.1016/j.tecto.2008.04.005.

Cathelineau, M., Boiron, M.-C., Fourcade, S., Ruffet, G., Clauer, N., Belcourt, O., Coulibaly, Y., Banks, D.A., Guillocheau, F., 2012. A major late Jurassic fluid event at the basin/basement unconformity in western France: 40Ar/39Ar and K–Ar dating, fluid chemistry, and related geodynamic context. Chem. Geol. 322–323, 99–120. https://doi.org/10.1016/j.chemgeo.2012.06.008.

Cawood, T.K., Platt, J.P., 2021. What controls the width of ductile shear zones? Tectonophysics 816, 229033. https://doi.org/10.1016/j.tecto.2021.229033.

Cross, A.J., Prior, D.J., Stipp, M., Kidder, S., 2017. The recrystallized grain size piezometer for quartz: an EBSD-based calibration. Geophys. Res. Lett. 44, 6667–6674. https://doi.org/10.1002/2017GL073836.

de Riese, T., Evans, L., Gomez-Rivas, E., Griera, A., Lebensohn, R.A., Llorens, M.-G., Ran, H., Sachau, T., Weikusat, I., Bons, P.D., 2019. Shear localisation in anisotropic, non-linear viscous materials that develop a CPO: a numerical study. J. Struct. Geol. 124, 81–90. https://doi.org/10.1016/j.jsg.2019.03.006.

Deloule, E., Alexandrov, P., Cheilletz, A., Laumonier, B., Barbey, P., 2002. In-situ U–Pb zircon ages for early Ordovician magmatism in the eastern Pyrenees, France: the Canigou orthogneisses. Int. J. Earth Sci. 91, 398–405. https://doi.org/10.1007/s00531-001-0232-0.

Den Brok, D.W.I., 1989. Evidence for pre-variscan deformation in the Lys Caillaouas area, Central Pyrenees, France. Geol. Mijnbouw 68, 377–380.

Denèle, Y., Olivier, P., Gleizes, G., 2008. Progressive deformation of a zone of magma transfer in a transpressional regime: the Variscan Mérens shear zone (Pyrenees, France). J. Struct. Geol. 30, 1138–1149. https://doi.org/10.1016/j.jsg.2008.05.006.

Domínguez-Carretero, D., Proenza, J.A., González-Jiménez, J.M., Llanes-Castro, A.I., Torres, H., Aiglsperger, T., Torró, L., Capote, C., Nuez, D. de la, Garcia-Casco, A., 2022. Ultramafic-hosted volcanogenic massive sulfide deposits from Cuban ophiolites. J. S. Am. Earth Sci. 119, 103991. https://doi.org/10.1016/j.jsames.2022.103991.

Druguet, E., 1997. The Structure of the NE Cap De Creus Peninsula Relationships with Metamorphism and Magmatism: Phd Thesis. Universitat Autònoma de Barcelona, Barcelona unpublished.

Druguet, E., Carreras, J., 2019. Folds and Shear Zones at Cap de Creus. Field Trip Guide XXXI Reunión De La Comisión De Tectónica - SGE, p. 27.

Druguet, E., Carreras, J., Mezger, J.E., 2018. Discussion on 'Middle Jurassic shear zones at Cap de Creus (eastern Pyrenees, Spain): a record of pre-drift extension of the Piemonte–Ligurian Ocean?'. J. Geological Soc. London 174, 289–300. https://doi.org/10.1144/jgs2017-042. Journal of the Geological Society, v. 175, pp. 187–188.

Druguet, E., Castro, A., Chichorro, M., Pereira, M.F., Fernández, C., 2014. Zircon geochronology of intrusive rocks from Cap de Creus, Eastern Pyrenees. Geol. Mag. 151, 1095–1114. https://doi.org/10.1017/S0016756814000041.

Dunlap, W.J., 1997. Neocrystallization or cooling? 40Ar/39Ar ages of white micas from low-grade mylonites. Chem. Geol. 143, 181–203. https://doi.org/10.1016/S0009-2541(97)00113-7.

Dunlap, W.J., Teyssier, C., McDougall, I., Baldwin, S., 1991. Ages of deformation from K/Ar and 40Ar/39Ar dating of white micas. Geology 19, 1213–1216. https://doi.org/10.1130/0091-7613(1991)019<1213:AODFKA>2.3.CO;2.

Dutta, D., Mukherjee, S., 2021. Extrusion kinematics of UHP terrane in a collisional orogen: EBSD and microstructure-based approach from the Tso Morari Crystallines (Ladakh Himalaya). Tectonophysics 800, 228641. https://doi.org/10.1016/j.tecto.2020.228641.

Fazio, E., Punturo, R., Cirrincione, R., Kern, H., Pezzino, A., Wenk, H.-R., Goswami, S., Mamtani, M.A., 2017. Quartz preferred orientation in naturally deformed mylonitic rocks (Montalto shear zone–Italy): a comparison of results by different techniques, their advantages and limitations. Int. J. Earth Sci. 106, 2259–2278. https://doi.org/10.1007/s00531-016-1424-y.

Finch, M.A., Weinberg, R.F., Hunter, N.J.R., 2016. Water loss and the origin of thick ultramylonites. Geology 44, 599–602. https://doi.org/10.1130/G37972.1.

Fonseca, H.A.M., Canals, A., Cirés, J., Casas, J.M., 2015. The Roses Giant Quartz Vein (Cap de Creus. Eastern Pyrenees): Geol. Fluid Inclusion Data: Macla v. 20, 49–50.

Forster, M.A., Lister, G.S., 2004. The interpretation of 40Ar/39Ar apparent age spectra produced by mixing: application of the method of asymptotes and limits. J. Struct. Geol. 26, 287–305. https://doi.org/10.1016/j.jsg.2003.10.004.

Fossen, H., Cavalcante, G.C.G., 2017. Shear zones – a review. Earth Sci. Rev. 171, 434–455. https://doi.org/10.1016/j.earscirev.2017.05.002.

Fusseis, F., Handy, M.R., Schrank, C., 2006. Networking of shear zones at the brittle-to-viscous transition (Cap de Creus, NE Spain). J. Struct. Geol. 28 (7), 1228–1243. https://doi.org/10.1016/j.jsg.2006.03.022.

Gerdes, A., Zeh, A., 2006. Combined U-Pb and Hf isotope LA-(MC-)ICP-MS analyses of detrital zircons: comparison with SHRIMP and new constraints for the provenance and age of an Armorican metasediment in Central Germany. Earth Planet Sci. Lett. 249, 47–61. https://doi.org/10.1016/j.epsl.2006.06.039.

Gerdes, A., Zeh, A., 2009. Zircon formation versus zircon alteration — new insights from combined U-Pb and Lu-Hf in-situ LA-ICP-MS analyses, and consequences for the interpretation of Archean zircon from the Central Zone of the Limpopo Belt. Chem. Geol. 261, 230–243. https://doi.org/10.1016/j.chemgeo.2008.03.005.

González-Esvertit, E., Canals, À., Bons, P.D., Casas, J.M., Gomez-Rivas, E., 2022a. Compiling regional structures in geological databases: the giant quartz veins of the Pyrenees as a case study. J. Struct. Geol. 163, 104705. https://doi.org/10.1016/j.jsg.2022.104705.

González-Esvertit, E., 2025. Fluid migration, rock deformation, and mineral alteration in the Earth's crust. Insights from Giant Quartz Veins and their Host Rocks in the Pyrenees. University of Barcelona, 442p. PhD thesis. doi:10803/695044.

González-Esvertit, E., Canals, A., Bons, P.D., Casas, J.M., Nieto, F., Gomez-Rivas, E., 2024. Chlorite chemical refinement during giant quartz vein formation. GSA Bullet. 136 (11–12), 5208–5216. https://doi.org/10.1130/B37510.1.

González-Esvertit, E., Canals, À., Bons, P.D., Murta, H., Casas, J.M., Gomez-Rivas, E., 2022b. Geology of giant quartz veins and their host rocks from the Eastern Pyrenees (Southwest Europe). J. Maps 19, 1–13. https://doi.org/10.1080/17445647.2022.2133642.

González-Esvertit, E., Canals, A., Prieto-Torrell, C., Bons, P.D., Llorens, M.-G., Casas, J.M., Aguilar, C., Neilson, J., Elburg, M.A., Gomez-Rivas, E., 2025a. Granitoid metasomatism and giant quartz vein formation by mineral replacement: insights from the Canigó Massif, Eastern Pyrenees. J. Petrol. 66 (2), egaf007. https://doi.org/10.1093/petrology/egaf007.

González-Esvertit, E., Fusswinkel, T., Canals, A., Casas, J.M., Neilson, J., Wagner, T., Gomez-Rivas, E., 2025b. Fluid evolution and halogen fractionation in orogenic belts: a comparative fluid inclusion appraisal in the Eastern Pyrenees. Chem. Geol. 674, 122578. https://doi.org/10.1016/j.chemgeo.2024.122578.

González-Esvertit, E., Prieto-Torrell, C., Bons, P.D., Canals, A., Casas, J.M., Elburg, M.A., Gomez-Rivas, E., 2025c. A review of the granite concept through time. Earth Sci. Rev. 261, 105008. https://doi.org/10.1016/j.earscirev.2024.105008.

González-Esvertit, E., Molins-Vigatà, J., Canals, À., Casas, J.M., 2023. The geology of the Gréixer area (La Cerdanya, Eastern Pyrenees): Sardic, Variscan, and Alpine imprints. Trab. Geol. 37 (37), 81–95. https://doi.org/10.17811/tdg.37.2023.81-95.

Griera, A., Bons, P.D., Jessell, M.W., Lebensohn, R.A., Evans, L., Gomez-Rivas, E., 2011. Strain localization and porphyroclast rotation. Geology 39, 275–278. https://doi.org/10.1130/G31549.1.

Guitard, G., 1965. Carte Géologique des Massifs du Canigou et de la Carançà à 1/50.000. BRGM, v. Service de la Carte Géologique de France.

Guitard, G., 1953. La structure du massif du Canigou; apercu sur le metamorphisme regional dans la zone axiale des Pyrenees orientales (note preliminare). Bull. Soc. Geol. Fr. 6, 907–924 [with discussion].

Guitard, G., 1970. Le métamorphisme hercynien mésozonal et les gneiss oeillés du massif du Canigou (Pyrénées orientales). Mémoires du Bureau de Recherches Géologiques et Minières (BRGM) v. 63, 353.

Guitard, G., 1955. Sur l'evolution des gneiss des Pyrenees. Bull. Soc. Geol. Fr. S6-V, 441–469. https://doi.org/10.2113/gssgfbull.S6-V.7-9.441.

Guitard, G., Laumonier, B., Autran, A., Bandet, Y., Berger, G., 1998. Notice Explicative De La Feuille Prats-de-Mollo-La-Preste À 1/50,000: BRGM Éditions-Service Géologique National, p. 193.

Handy, M.R., 1990. The solid-state flow of polymineralic rocks. J. Geophys. Res. Solid Earth 95 (B6), 8647–8661. https://doi.org/10.1029/JB095iB06p08647.

Hao, B., Llorens, M.-G., Griera, A., Bons, P.D., Lebensohn, R.A., Yu, Y., Gomez-Rivas, E., 2023. Full-field numerical simulation of halite dynamic recrystallization from subgrain rotation to grain boundary migration. J. Geophys. Res. Solid Earth 128, e2023JB027590. https://doi.org/10.1029/2023JB027590.

Harrison, T.M., Célérier, J., Aikman, A.B., Hermann, J., Heizler, M.T., 2009. Diffusion of 40Ar in muscovite. Geochem. Cosmochim. Acta 73, 1039–1051.

Heilbronner, R., Tullis, J., 2006. Evolution of c axis pole figures and grain size during dynamic recrystallization: results from experimentally sheared quartzite. J. Geophys. Res. Solid Earth 111.

Hippertt, J.F., 1994. Microstructures and c-axis fabrics indicative of quartz dissolution in sheared quartzites and phyllonites. Tectonophysics 229, 141–163.

Hirth, G., Tullis, J., 1992. Dislocation creep regimes in quartz aggregates. J. Struct. Geol. 14, 145–159. https://doi.org/10.1016/0191-8141(92)90053-Y.

Horstwood, M.S.A., Košler, J., Gehrels, G., Jackson, S.E., McLean, N.M., Paton, C., Pearson, N.J., Sircombe, K., Sylvester, P., Vermeesch, P., Bowring, J.F., Condon, D.J., Schoene, B., 2016. Community-derived standards for LA-ICP-MS U-(Th-)Pb geochronology – uncertainty propagation, age interpretation and data reporting. Geostand. Geoanal. Res. 40, 311–332. https://doi.org/10.1111/j.1751-908X.2016.00379.x.

Hu, Y.B., Bons, P.D., de Riese, T., Liu, S.G., Llorens, M.G., González-Esvertit, E., et al., 2024. Folding of a single layer in an anisotropic viscous matrix under layer-parallel shortening. J. Struct. Geol. 188, 105246. https://doi.org/10.1016/j.jsg.2024.105246.

Hunter, N.J.R., Hasalová, P., Weinberg, R.F., Wilson, C.J.L., 2016. Fabric controls on strain accommodation in naturally deformed mylonites: the influence of interconnected micaceous layers. J. Struct. Geol. 83, 180–193. https://doi.org/10.1016/j.jsg.2015.12.005.

Hunter, N.J.R., Weinberg, R.F., Wilson, C.J.L., Luzin, V., Misra, S., 2019. Quartz deformation across interlayered monomineralic and polymineralic rocks: a comparative analysis. J. Struct. Geol. 119, 118–134. https://doi.org/10.1016/j.jsg.2018.12.005.

Jackson, S.E., Pearson, N.J., Griffin, W.L., Belousova, E.A., 2004. The application of laser ablation-inductively coupled plasma-mass spectrometry to in situ U–Pb zircon geochronology. Chem. Geol. 211, 47–69. https://doi.org/10.1016/j.chemgeo.2004.06.017.

Keulen, N., Heilbronner, R., Stünitz, H., Boullier, A.-M., Ito, H., 2007. Grain size distributions of fault rocks: a comparison between experimentally and naturally deformed granitoids. J. Struct. Geol. 29, 1282–1300. https://doi.org/10.1016/j.jsg.2007.04.003.

Kilian, R., Heilbronner, R., 2017. Analysis of crystallographic preferred orientations of experimentally deformed black hills quartzite. Solid Earth 8, 1095–1117. https://doi.org/10.5194/se-8-1095-2017, 2017.

Kilian, R., Heilbronner, R., Stünitz, H., 2011a. Quartz grain size reduction in a granitoid rock and the transition from dislocation to diffusion creep. J. Struct. Geol. 33, 1265–1284. https://doi.org/10.1016/j.jsg.2011.05.004.

Kilian, R., Heilbronner, R., Stünitz, H., 2011b. Quartz microstructures and crystallographic preferred orientation: which shear sense do they indicate? J. Struct. Geol. 33, 1446–1466. https://doi.org/10.1016/j.jsg.2011.08.005.

Kirschner, D.L., Cosca, M.A., Masson, H., Hunziker, J.C., 1996. Staircase 40/Ar39Ar spectra of fine-grained white mica: timing and duration of deformation and empirical constraints on argon diffusion. Geology 24, 747–750. https://doi.org/10.1130/0091-7613(1996)024<0747:SAASOF>2.3.CO;2.

Koppers, A.A.P., 2002. ArArCALC—software for 40Ar/39Ar age calculations. Comput. Geosci. 28, 605–619. https://doi.org/10.1016/S0098-3004(01)00095-4.

Kronenberg, A.K., Segall, P., Wolf, G.H., 1990. Hydrolytic weakening and penetrative deformation within a natural shear zone: the brittle-ductile transition in rocks, 56, 21–36.

Kruhl, J.H., 1996. Prism-and basal-plane parallel subgrain boundaries in quartz: a microstructural geothermobarometer. J. Metamorph. Geol. 14, 581–589.

Kuiper, K.F., Deino, A., Hilgen, F.J., Krijgsman, W., Renne, P.R., Wijbrans, J.R., 2008. Synchronizing rock clocks of Earth history. Science 320, 500–504. https://doi.org/10.1126/science.1154339.

Kula, J., Spell, T.L., Zanetti, K.A., 2010. 40Ar/39Ar analyses of artificially mixed micas and the treatment of complex age spectra from samples with multiple mica populations. Chem. Geol. 275, 67–77. https://doi.org/10.1016/j.chemgeo.2010.04.015.

Lacroix, A., 1898. Le granite des Pyrénées et ses phénomènes de contact. In: Bull. Carte Gdol, 64. Librairie polytechnique, France.

Lacroix, M.A., 1920. Les Roches Éruptives Du Crétace Pyrénéen Et la Nomenclature Des Roches Éruptives Modifiées: Comptes Rendues Acad Sci France, 170, pp. 685–690.

Lacroix, A., 1896. Les Transformations Endomorphiques Du Magma Granitique Dans La Haute Ariege, Au Contact Des Calcaires, 123. Comptes Rendus de l'Académie des sciences France, pp. 1021–1023.

Laumonier, B., 1988. Les groupes de Canaveilles et de Jujols ("'Paléozoïque inférieur"') des Pyrénées orientales – arguments en faveur de l'âge essentiellement Cambrien de ces séries. Hercynica 4, 25–38.

Laumonier, B., Calvet, M., Bayon, B.L., Barbey, P., 2015. Notice Explicative De La Feuille Prats-de-Mollo-La-Preste À 1/50,000: BRGM Éditions-Service Géologique National, p. 193.

Law, R.D., 1987. Heterogeneous deformation and quartz crystallographic fabric transitions: natural examples from the Moine Thrust zone at the stack of glencoul, northern assynt. J. Struct. Geol. 9, 819–833.

Law, R.D., Schmid, S.M., Wheeler, J., 1990. Simple shear deformation and quartz crystallographic fabrics: a possible natural example from the torridon area of NW Scotland. J. Struct. Geol. 12, 29–45. https://doi.org/10.1016/0191-8141(90)90046-2.

Le Bayon, B., Cochelin, B., 2020. Anatomy of an extensional shear zone leading to the exhumation of the middle crust within the Canigou dome (Eastern Pyrenees, Axial Zone). J. Struct. Geol. 141, 104200. https://doi.org/10.1016/j.jsg.2020.104200.

Lee, A.L., Lloyd, G.E., Torvela, T., Walker, A.M., 2020. Evolution of a shear zone before, during and after melting. J. Geol. Soc. 177, 738–751. https://doi.org/10.1144/jgs2019-114.

Lemirre, B., Cochelin, B., Duchene, S., de Saint Blanquat, M., Poujol, M., 2019. Origin and duration of late orogenic magmatism in the foreland of the Variscan belt (Lesponne — Chiroulet — neouvielle area, French Pyrenees). Lithos 336–337, 183–201. https://doi.org/10.1016/j.lithos.2019.03.037.

Liesa, M., Aguilar, C., Castro, A., Gisbert, G., Reche, J., Muñoz, J.A., Vilà, M., 2021. The role of mantle and crust in the generation of calc-alkaline Variscan magmatism and its tectonic setting in the Eastern Pyrenees. Lithos 406–407, 106541. https://doi.org/10.1016/j.lithos.2021.106541.

Liesa, M., Carreras, J., 1989. On the Structure and Metamorphism of the Roc de Frausa Massif (Eastern Pyrenees). Geodin. Acta 3, 149–161. https://doi.org/10.1080/09853111.1989.11105182.

Lister, G.S., Williams, P.F., 1979. Fabric development in shear zones: theoretical controls and observed phenomena. J. Struct. Geol. 1, 283–297. https://doi.org/10.1016/0191-8141(79)90003-8.

Lister, G.S., Williams, P.F., 1983. The partitioning of deformation in flowing rock masses. Tectonophysics 92, 1–33. https://doi.org/10.1016/0040-1951(83)90083-5.

Llorens, M.-G., Bons, P.D., Griera, A., Gomez-Rivas, E., 2013. When do folds unfold during progressive shear? Geology 41, 563–566. https://doi.org/10.1130/G33973.1.

Llorens, M.-G., Gomez-Rivas, E., Ganzhorn, A.-C., Griera, A., Steinbach, F., Roessiger, J., Labrousse, L., Walte, N.P., Weikusat, I., Bons, P.D., 2019. The effect of dynamic recrystallisation on the rheology and microstructures of partially molten rocks. J. Struct. Geol. 118, 224–235. https://doi.org/10.1016/j.jsg.2018.10.013.

Losantos, M., Palau, J., Carreras, J., Druguet, E., Santanach, P., Cirés, J., 1997. Mapa Geològic De Catalunya a Escala 1:25.000, Hoja 259-1-1(79-21)-Roses. Institut Cartogràfic i Geològic de Catalunya.

Ludwig, K.R., 2012. User's Manual for Isoplot Version 3.75-4.15: a Geochronological Toolkit for Microsoft Excel, 5. Berkeley Geochronological Center Special Publication.

Macchiavelli, C., Vergés, J., Schettino, A., Fernàndez, M., Turco, E., Casciello, E., Torne, M., Pierantoni, P.P., Tunini, L., 2017. A new Southern north Atlantic isochron map: insights into the drift of the Iberian plate since the Late Cretaceous. J. Geophys. Res. 24.

Majoor, F.J.M., 1988. A Geochronological Study of the Axial Zone of the Central Pyrenees, with Emphasis on Variscan Events and Alpine Resetting: Verhandeling Nr. 6 Zwo Laboratorium Voor Isotopen-Geologie, vols. 1–117. Amsterdam.

Mancktelow, N.S., 1987. Quartz textures from the Simplon fault zone, southwest Switzerland and north Italy. Tectonophysics 135, 133–153. https://doi.org/10.1016/0040-1951(87)90157-0.

Mancktelow, N.S., Pennacchioni, G., 2004. The influence of grain boundary fluids on the microstructure of quartz-feldspar mylonites. J. Struct. Geol. 26, 47–69. https://doi.org/10.1016/S0191-8141(03)00081-6.

Mandal, N., Misra, S., Kumar Samanta, S., 2004. Role of weak flaws in nucleation of shear zones: an experimental and theoretical study. J. Struct. Geol. 26, 1391–1400. https://doi.org/10.1016/j.jsg.2004.01.001.

Margalef, A., Granado, P., Casas, J.M., 2023. Superposed Variscan and Alpine deformation in the basement rocks of southern Andorra, Central Pyrenees. J. Geol. Soc. 0, jgs2023–j2099. https://doi.org/10.1144/jgs2023-099.

Martín-Closas, C., Trias, S., Casas, J.M., 2018. New palaeobotanical data from Carboniferous Culm deposits constrain the age of the Variscan deformation in the eastern Pyrenees. Geol. Acta 16, 107–123. https://doi.org/10.1344/GeologicaActa2018.16.2.1.

Martínez, F.J., Iriondo, A., Dietsch, C., Aleinikoff, J.N., Peucat, J.J., Cirès, J., Reche, J., Capdevila, R., 2011. U-Pb SHRIMP-RG zircon ages and Nd signature of lower Paleozoic rifting-related magmatism in the Variscan basement of the Eastern Pyrenees. Lithos 127, 10–23. https://doi.org/10.1016/j.lithos.2011.08.004.

Maurel, O., 2003. L'Exhumation De La Zone Axiale Des Pyrénées Orientales : Une Approche Thermochronologique multi-méthodes Du Rôle Des Failles.

Maurel, O., Monié, P., Pik, R., Arnaud, N., Brunel, M., Jolivet, M., 2008. The Meso-Cenozoic thermo-tectonic evolution of the Eastern Pyrenees: an 40Ar/39Ar fission track and (U–Th)/He thermochronological study of the Canigou and Mont-Louis massifs. Int. J. Earth Sci. 97, 565–584. https://doi.org/10.1007/s00531-007-0179-x.

McCaig, A.M., Miller, J.A., 1986. 40Ar-39Ar age of mylonites along the Merens fault, central Pyrenees. Tectonophysics 129, 149–172.

McCaig, A.M., Tritlla, J., Banks, D.A., 2000a. Fluid mixing and recycling during pyrenean thrusting: evidence from fluid inclusion halogen ratios. Geochem. Cosmochim. Acta 64, 3395–3412. https://doi.org/10.1016/S0016-7037(00)00437-3.

McCaig, A.M., Wayne, D.M., Rosenbaum, J.M., 2000b. Fluid expulsion and dilatancy pumping during thrusting in the Pyrenees: pb and Sr isotope evidence. GSA Bullet. 112, 1199–1208. https://doi.org/10.1130/0016-7606(2000)112<1199:FEADPD>2.0.CO;2.

McCaig, A.M., Wickham, S.M., Taylor, H.P., 1990. Deep fluid circulation in alpine shear zones, Pyrenees, France: field and oxygen isotope studies. Contrib. Mineral. Petrol. 106, 41–60. https://doi.org/10.1007/BF00306407.

Menegon, L., Pennacchioni, G., Heilbronner, R., Pittarello, L., 2008. Evolution of quartz microstructure and *c*-axis crystallographic preferred orientation within ductilely deformed granitoids (Arolla unit, Western Alps). J. Struct. Geol. 30, 1332–1347. https://doi.org/10.1016/j.jsg.2008.07.007.

Mezger, J., Gerdes, A., 2016. Early Variscan (Visean) granites in the core of central pyrenean gneiss domes: implications from laser ablation U-Pb and Th-Pb studies. Gondwana Res. 29, 181–198. https://doi.org/10.1016/j.gr.2014.11.010.

Mezger, J.E., Schnapperelle, S., Rölke, C., 2012. Evolution of the Central Pyrenean Mérens Fault Controlled by near Collision of Two Gneiss Domes: Hallesches Jahrbuch Für Geowissenschaften, 34, pp. 11–30. https://doi.org/10.25673/91866.

Michel-Lévy, A., 1889. Structures et classification des roches éruptives: Librairie Polytechnique, Baudry et cie. Éditeurs, p. 114.

Min, K., Mundil, R., Renne, P.R., Ludwig, K.R., 2000. A test for systematic errors in 40Ar/39Ar geochronology through comparison with U/Pb analysis of a 1.1-Ga rhyolite. Geochem. Cosmochim. Acta 64, 73–98. https://doi.org/10.1016/S0016-7037(99)00204-5.

Monié, P., Oliot, É., Milesi, G., Allard, M., Faucher, A., 2025. 40Ar/39Ar dating of poly-orogenic rocks: an example from the Cap de Creus peninsula (Eastern Pyrenees, Spain). J. Struct. Geol., 105489 https://doi.org/10.1016/j.jsg.2025.105489.

Monie, P., Soliva, J., Brunel, M., Maluski, H., 1994. Les cisaillements mylonitiques du granite de Millas (Pyrenees, France); age Cretace 40 Ar/39 Ar et interpretation tectonique. Bull. Soc. Geol. Fr. 165, 559–571.

Muñoz, J.A., 1992. Evolution of a continental collision belt: ECORS-Pyrenees crustal balanced cross-section. In: McClay, K.R. (Ed.), Thrust Tectonics. Springer Netherlands, Dordrecht, pp. 235–246. https://doi.org/10.1007/978-94-011-3066-0_21.

Navidad, M., Castiñeiras, P., Casas, J.M., Liesa, M., Belousova, E., Proenza, J., Aiglsperger, T., 2018. Ordovician magmatism in the Eastern Pyrenees: implications for the geodynamic evolution of northern Gondwana. Lithos 314–315, 479–496. https://doi.org/10.1016/j.lithos.2018.06.019.

Navidad, M., Castiñeiras, P., Casas, J.M., Liesa, M., Fernández Suárez, J., Barnolas, A., Carreras, J., Gil-Peña, I., 2010. Geochemical characterization and isotopic age of Caradocian magmatism in the northeastern Iberian Peninsula: insights into the late Ordovician evolution of the northern Gondwana margin. Gondwana Res. 17, 325–337. https://doi.org/10.1016/j.gr.2009.11.013.

Neves, S.P., Vauchez, A., Archanjo, C.J., 1996. Shear zone-controlled magma emplacement or magma-assisted nucleation of shear zones? Insights from northeast Brazil. Tectonophysics 262, 349–364. https://doi.org/10.1016/0040-1951(96)00007-8.

Oliot, E., Goncalves, P., Schulmann, K., Marquer, D., Lexa, O., 2014. Mid-crustal shear zone formation in granitic rocks: constraints from quantitative textural and crystallographic preferred orientations analyses. Tectonophysics 612–613, 63–80. https://doi.org/10.1016/j.tecto.2013.11.032.

Olivier, P., Druguet, E., Castaño, L.M., Gleizes, G., 2016. Granitoid emplacement by multiple sheeting during Variscan dextral transpression: the Saint-Laurent – La Jonquera pluton (Eastern Pyrenees). J. Struct. Geol. 82, 80–92. https://doi.org/10.1016/j.jsg.2015.10.006.

Oriolo, S., Wemmer, K., Oyhantçabal, P., Fossen, H., Schulz, B., Siegesmund, S., 2018. Geochronology of shear zones – a review. Earth Sci. Rev. 185, 665–683. https://doi.org/10.1016/j.earscirev.2018.07.007.

Padel, M., Clausen, S., Álvaro, J.J., Casas, J.M., 2018. Review of the Ediacaran-Lower Ordovician (pre-Sardic) stratigraphic framework of the Eastern Pyrenees, southwestern Europe. Geol. Acta 16, 339–365.

Passchier, C.W., Trouw, R.A.J., 1996. Microtectonics. Springer Verlag, Berlin.

Pennacchioni, G., Cesare, B., 1997. Ductile-brittle transition in pre-alpine amphibolite facies mylonites during evolution from water-present to water-deficient conditions (Mont Mary nappe, Italian Western Alps). J. Metamorph. Geol. 15, 777–791. https://doi.org/10.1111/j.1525-1314.1997.00055.x.

Pennacchioni, G., Zucchi, E., 2013. High temperature fracturing and ductile deformation during cooling of a pluton: the Lake Edison granodiorite (Sierra Nevada batholith, California). J. Struct. Geol. 50, 54–81. https://doi.org/10.1016/j.jsg.2012.06.001.

Peternell, M., Hasalová, P., Wilson, C.J.L., Piazolo, S., Schulmann, K., 2010. Evaluating quartz crystallographic preferred orientations and the role of deformation partitioning using EBSD and fabric analyser techniques. J. Struct. Geol. 32, 803–817. https://doi.org/10.1016/j.jsg.2010.05.007.

Pitra, P., Martínez, F.J., 2024. Incomplete Hydration during 'Retrograde' Metamorphism: 'barrovian' Kyanite-, Staurolite-, Chloritoid-Bearing Pseudomorphs after Andalusite (Cap de Creus, E Pyrenees, Spain). J. Petrol. 65, egae004. https://doi.org/10.1093/petrology/egae004.

Post, A., Tullis, J., 1998. The rate of water penetration in experimentally deformed quartzite: implications for hydrolytic weakening. Tectonophysics 295, 117–137. https://doi.org/10.1016/S0040-1951(98)00145-0.

Puddu, C., Álvaro, J.J., Carrera, N., Casas, J.M., 2019. Deciphering the Sardic (Ordovician) and Variscan deformations in the Eastern Pyrenees, SW Europe. J. Geol. Soc. 176, 1191–1206. https://doi.org/10.1144/jgs2019-057.

Pujol-Solà, N., Domínguez-Carretero, D., Proenza, J.A., Haissen, F., Ikenne, M., González-Jiménez, J.M., Colás, V., Maacha, L., Garcia-Casco, A., 2021. The chromitites of the Neoproterozoic Bou Azzer ophiolite (central Anti-Atlas, Morocco) revisited. Ore Geol. Rev. 134, 104166. https://doi.org/10.1016/j.oregeorev.2021.104166.

Purdy, J.W., 1976. K-Ar ages on rock forming minerals from the Central Alps: memorie degli Istituti di Geologia e Mineralogia dell'Università di Padova, 30, 1–31.

Ramsay, J.G., Graham, R.H., 1970. Strain variation in shear belts. Can. J. Earth Sci. 7, 786–813. https://doi.org/10.1139/e70-078.

Ran, H., et al., 2019. Time for anisotropy: the significance of mechanical anisotropy for the development of deformation structures. J. Struct. Geol. 125, 41–47. https://doi.org/10.1016/j.jsg.2018.04.019.

Roest, W.R., Srivastava, S.P., 1991. Kinematics of the plate boundaries between Eurasia, Iberia, and Africa in the North Atlantic from the Late Cretaceous to the present. Geology 19, 613–616. https://doi.org/10.1130/0091-7613(1991)019<0613:KOTPBB>2.3.CO;2.

Rolland, Y., Rossi, M., Cox, S.F., Corsini, M., Mancktelow, N., Pennacchioni, G., Fornari, M., Boullier, A.M., 2008. 40Ar/39Ar Dating of Synkinematic White Mica: Insights from fluid-rock Reaction in low-grade Shear Zones (Mont Blanc Massif) and Constraints on Timing of Deformation in the NW External Alps, 299. Geological Society, London, Special Publications, pp. 293–315. https://doi.org/10.1144/SP299.18.

Rossi, P., Oggiano, G., Cocherie, A., 2009. A restored section of the "southern Variscan realm" across the Corsica–Sardinia microcontinent. C. R. Geosci. 341, 224–238. https://doi.org/10.1016/j.crte.2008.12.005.

Russo, D., Fiannacca, P., Fazio, E., Cirrincione, R., Mamtani, M.A., 2022. From floor to roof of a batholith: geology and petrography of the north-eastern Serre Batholith (Calabria, southern Italy). J. Maps 0, 1–15. https://doi.org/10.1080/17445647.2022.2149358.

Salomon, E., Koehn, D., Passchier, C., 2015. Brittle reactivation of ductile shear zones in NW Namibia in relation to South Atlantic rifting. Tectonics 34, 70–85. https://doi.org/10.1002/2014TC003728.

Santanach, P., 1972a. Estudio Tectónico Del Paleozoico Inferior Del Pirineo Entre La Cerdaña Y El Río Ter, 7. Acta Geologica Hispanica, pp. 44–49.

Santanach, P., 1972b. Sobre Una Discordancia En El Paleozoico Inferior De Los Pirineos Orientales, 7. Acta Geologica Hispanica, pp. 129–132.

Santos, M.M., Lana, C., Scholz, R., Buick, I., Schmitz, M.D., Kamo, S.L., Gerdes, A., Corfu, F., Tapster, S., Lancaster, P., Storey, C.D., Basei, M.A., Tohver, E., Alkmim, A., Nalini, H., Krambrock, K., Fantini, C., Wiedenbeck, M., 2017. A new appraisal of Sri Lankan BB zircon as a reference material for LA-ICP-MS U-Pb geochronology and Lu-Hf isotope tracing. Geostand. Geoanal. Res. 41, 335–358. https://doi.org/10.1111/ggr.12167.

Schaen, A.J., et al., 2020. Interpreting and reporting 40Ar/39Ar geochronologic data. GSA Bullet. 133, 461–487. https://doi.org/10.1130/B35560.1.

Schmid, S.M., Casey, M., 1986. Complete fabric analysis of some commonly observed quartz C-Axis patterns. In: Mineral and Rock Deformation. American Geophysical Union (AGU), pp. 263–286. https://doi.org/10.1029/GM036p0263.

Schneider, S., Hammerschmidt, K., Rosenberg, C.L., 2013. Dating the longevity of ductile shear zones: insight from 40Ar/39Ar in situ analyses. Earth Planet Sci. Lett. 369–370, 43–58. https://doi.org/10.1016/j.epsl.2013.03.002.

Shigematsu, N., Prior, D.J., Wheeler, J., 2006. First combined electron backscatter diffraction and transmission electron microscopy study of grain boundary structure of deformed quartzite. J. Microsc. 224 (3), 306–321.

Sibson, R.H., 1977. Fault rocks and fault mechanisms. J. Geol. Soc. 133, 191–213. https://doi.org/10.1144/gsjgs.133.3.0191.

Simpson, C., 1985. Deformation of granitic rocks across the brittle-ductile transition. J. Struct. Geol. 7, 503–511.

Simpson, C., De Paor, D.G., 1993. Strain and kinematic analysis in general shear zones. J. Struct. Geol. 15, 1–20. https://doi.org/10.1016/0191-8141(93)90075-L.

Skemer, P., Warren, J.M., Kelemen, P.B., hirth, G., 2010. Microstructural and rheological evolution of a mantle shear zone. J. Petrol. 51, 43–53. https://doi.org/10.1093/petrology/egp057.

Slama, J., Kosler, J., Condon, D.J., Crowley, J.L., Gerdes, A., Hanchar, J.M., Horstwood, M.S.A., Morris, G.A., Nasdala, L., Norberg, N., Schaltegger, U., Schoene, B., Tubrett, M.N., Whitehouse, M.J., 2008. Plesovice zircon - a new natural reference material for U–Pb and Hf isotopic microanalysis. Chem. Geol. 249, 1–35. https://doi.org/10.1016/j.chemgeo.2007.11.005.

Soula, J.C., Lamouroux, C., Viallard, P., Bessiére, G., Debat, P., Ferret, B., 1986. The Mylonite zones in the pyrenees and their place in the alpine tectonic evolution. Tectonophysics 129, 115–147. https://doi.org/10.1016/0040-1951(86)90249-0.

Stipp, M., Stünitz, H., Heilbronner, R., Schmid, S.M., 2002. Dynamic Recrystallization of Quartz: Correlation Between Natural and Experimental Conditions, 200. Geological Society, London, Special Publications, pp. 171–190. https://doi.org/10.1144/GSL.SP.2001.200.01.11.

Tavani, S., Bertok, C., Granado, P., Piana, F., Salas, R., Vigna, B., Muñoz, J.A., 2018. The Iberia-Eurasia plate boundary east of the Pyrenees. Earth Sci. Rev. 187, 314–337. https://doi.org/10.1016/j.earscirev.2018.10.008.

Tokle, L., Hirth, G., Stünitz, H., 2023. The effect of muscovite on the microstructural evolution and rheology of quartzite in general shear. J. Struct. Geol. 169, 104835. https://doi.org/10.1016/j.jsg.2023.104835.

Toy, V.G., Prior, D.J., Norris, R.J., 2008. Quartz fabrics in the alpine fault mylonites: influence of pre-existing preferred orientations on fabric development during progressive uplift. J. Struct. Geol. 30, 602–621. https://doi.org/10.1016/j.jsg.2008.01.001.

Tullis, J., Yund, R.A., 1989. Hydrolytic weakening of quartz aggregates: the effects of water and pressure on recovery. Geophys. Res. Lett. 16, 1343–1346. https://doi.org/10.1029/GL016i011p01343.

Vauchez, A., Tommasi, A., Mainprice, D., 2012. Faults (shear zones) in the Earth's mantle. Tectonophysics 558–559, 1–27. https://doi.org/10.1016/j.tecto.2012.06.006.

Vergés, J., et al., 2019. An introduction to the alpine cycle in Iberia. In: Quesada, C., Oliveira, J.T. (Eds.), The Geology of Iberia: a Geodynamic Approach. Springer International Publishing, Regional Geology Reviews, Cham, pp. 1–14. https://doi.org/10.1007/978-3-030-11295-0_1.

Vilà, M., Pin, C., Liesa, M., Enrique, P., 2007. LPHT metamorphism in a late orogenic transpressional setting, albera massif, NE Iberia: implications for the geodynamic evolution of the variscan pyrenees. J. Metamorph. Geol. 25, 321–347. https://doi.org/10.1111/j.1525-1314.2007.00698.x.

Villa, I.M., Bucher, S., Bousquet, R., Kleinhanns, I.C., Schmid, S.M., 2014. Dating polygenetic metamorphic assemblages along a transect across the Western alps. J. Petrol. 55, 803–830. https://doi.org/10.1093/petrology/egu007.

Vissers, R.L.M., Drury, M.R., HoogerduijnStrating, E.H., Spiers, C.J., van der Wal, D., 1995. Mantle shear zones and their effect on lithosphere strength during continental breakup. Tectonophysics 249, 155–171. https://doi.org/10.1016/0040-1951(95)00033-J.

Vissers, R.L.M., Ganerød, M., Pennock, G.M., van Hinsbergen, D.J.J., 2020. Eocene seismogenic reactivation of a Jurassic ductile shear zone at Cap de Creus, Pyrenees, NE Spain. J. Struct. Geol. 134, 103994. https://doi.org/10.1016/j.jsg.2020.103994.

Vissers, R.L.M., van Hinsbergen, D.J.J., Meijer, P.Th, Piccardo, G.B., 2013. Kinematics of Jurassic ultra-slow spreading in the Piemonte Ligurian ocean. Earth Planet Sci. Lett. 380, 138–150. https://doi.org/10.1016/j.epsl.2013.08.033.

Vissers, R.L.M., van Hinsbergen, D.J.J., Wilkinson, C.M., Ganerød, M., 2017. Middle Jurassic shear zones at Cap de Creus (eastern Pyrenees, Spain): a record of pre-drift extension of the Piemonte–Ligurian Ocean? J. Geol. Soc. 174, 289–300. https://doi.org/10.1144/jgs2016-014.

Warr, L.N., 2021. IMA–CNMNC approved mineral symbols. Mineral. Mag. 85, 291–320. https://doi.org/10.1180/mgm.2021.43.

White, S.H., Burrows, S.E., Carreras, J., Shaw, N.D., Humphreys, F.J., 1980. On mylonites in ductile shear zones. J. Struct. Geol. 2, 175–187. https://doi.org/10.1016/0191-8141(80)90048-6.

Zwart, H.J., 1986. The variscan geology of the Pyrenees. Tectonophysics 129, 9–27. https://doi.org/10.1016/0040-1951(86)90243-X.